

**Department of Physics and Astronomy
Heidelberg University**

Bachelor Thesis in Physics

submitted by

Adrian Schürg

born in Ludwigsburg (Germany)

2024

Optimisation of microsecond laser pulses for lithium absorption imaging

This Bachelor Thesis has been carried out by

Adrian Schürg

at the Physikalisches Institut of the University of Heidelberg
under the supervision of

Prof. Dr. Lauriane Chomaz

Abstract

Our experiment aims to study the polaron scenario in an ultracold mixture of fermionic lithium and bosonic caesium at a relatively high magnetic field of around 900G. This requires precise imaging techniques, in order to reliably obtain relevant system parameters, such as the temperature. Employing low intensity absorption imaging for ${}^6\text{Li}$ for this task comes with challenges in terms of mitigating potential noise sources, most importantly photon shot noise and read out noise from the CCD camera. Therefore, this thesis investigates a theoretical model for the signal-to-noise ratio of our absorption imaging setup, resulting in finding the optimal imaging parameters, that maximise the signal-to-noise ratio, while also satisfying limits due to the Doppler effect and a random walk. In addition, we perform a scan over the imaging parameters, while determining the SNR, confirming these findings of our theoretical model. Furthermore two improvements to the setup are presented. A fibre monitoring system, that allows for tracking of the imaging pulses' optical power and a two-frequency AOM driver, which reduces thermalisation effects inside the AOM's crystal by employing two RF frequencies. We conduct several measurements regarding the driver's characteristics as well as long-term drifts in the optical power.

Zusammenfassung

Unser Experiment zielt darauf ab, in einem ultrakalten Gemisch aus fermionischem Lithium und bosonischem Caesium, bei einem magnetisch Feld von ca. 900G, Polaronen zu beobachten. Dazu erfordert es ein akkurates Abbildungssystem, um relevante Systemparameter wie die Temperatur zuverlässig zu erfassen. Hierfür verwenden wir für ${}^6\text{Li}$ die Absorptionsbildgebung bei niedrigen Intensitäten. Daher untersucht diese Arbeit ein theoretisches Modell für das Signal-Rausch-Verhältnis unseres Absorptionsbildgebungsaufbaus, um optimale Parameter, wie die Intesität und Belichtungsdauer zu finden, die das Signal-Rausch-Verhältnis maximieren und gleichzeitig Grenzen aufgrund des Dopplereffekts und eines Random Walks einhalten. Darüber hinaus führen wir einen Scan über die Aufbauparameter durch und bestimmen so das Signal-Rausch-Verhältnis für verschiedene Parameterkonfigurationen, und bestätigen damit die Ergebnisse unseres theoretischen Modells. Darüber hinaus werden zwei Verbesserungen des Aufbaus vorgestellt. Eine optisch Faser mit eingebauter photo diode, die Messungen der optischen Leistung der Laserpulse ermöglicht, und ein Zwei-Frequenz-AOM-Treiber, der thermische Effekte im Kristall des AOMs durch die Verwendung von zwei RF-Frequenzen reduziert. Wir führen mehrere Messungen zu den Eigenschaften des Treibers sowie zu potentiellen Langzeitdrifts in der optischen Leistung der Pulse durch.

Contents

Abstract

Zusammenfassung

1. Introduction	1
2. Absorption imaging	3
2.1. Imaging transition	3
2.2. Decay into dark states	8
2.3. Beer-Lambert law	10
3. Noise analysis	12
3.1. Doppler shift	12
3.2. Random walk	14
3.3. Optimal imaging parameters	15
4. Fibre monitoring	20
5. Dual Tone AOM	22
5.1. Setup for driving the AOM	23
5.2. Stability of long pulses	25
5.3. Stability of short pulses	26
5.4. Long-term drifts	28
6. Experimental results	29
6.1. Intensity calibration	29
6.2. Signal-to-noise ratio and comparison	31
7. Conclusion and Outlook	36
A. Appendix	38
A.1. Number of scattered photons	38
A.2. Experimental parameters	38
A.3. AOM driver components	39

A.4. AOM bandwidth	40
A.5. Long-term drifts	41
Bibliography	42
Acknowledgments	45
Statement of Authorship	46

1. Introduction

The study of quantum many body physics explores emergent properties of many interacting quantum particles, which often have no counterpart in classical systems. One area of particular interest is the field of ultracold-atomic quantum gases. To bridge the gap between quantum and classical regimes, theories like the polaron concept have been formulated. Originally formulated by Lev Landau in 1933, the polaron is a single impurity particle with a many-body background, forming a quasi-particle. Lev Landau described this in the context of an electron moving through a crystal lattice, that attracts nearby ionic crystal cores. Hence the electron drags along a cloud of polarisation as it moves through the crystal. The resulting quasi-particle consisting of the electron and its surrounding polarisation is called polaron. Other notable examples include investigations involving ^3He impurities immersed in a bosonic ^4He bath and the examination of the Kondo effect induced by localized magnetic impurities within metals.

In ultracold-atomic quantum gases, the polaron scenario can be realised as minority atoms (impurities) immersed in a majority atom bath, with interactions tunable by means of Feshbach resonances [1]. The designation of the quasi-particle as either a Fermi or Bose polaron depends on the quantum statistics exhibited by the atoms forming the surrounding bath. The first attractive Fermi polaron was realised with ^6Li atoms in 2009 [2]. Since then many other experiments successfully investigated the Fermi polaron [3, 4]. In 2016 the first Bose polaron was realised [5, 6].

The experiment, this thesis was conducted with, aims to investigate the polaron scenario in a mixture of fermionic lithium and bosonic caesium. This mixture is of particular interest, due to its high mass ratio of ~ 22 . This large mass imbalance enhances the Efimov effect, which led to observations of a series of Efimov states [7]. Building upon these investigations, delving into polaron physics is the next step. The polaron's ground state energy is strongly dependent on the temperature relative to the Fermi temperature T/T_F . Thus it is crucial to measure this parameter precisely, which is in our case done by means of imaging the fermionic lithium cloud by employing absorption imaging for this task.

The technique of absorption imaging serves as a fundamental tool in extracting phys-

ical quantities from a cloud of cold atoms and is widely used [8, 9, 10]. It operates based on the Beer-Lambert law, which describes how a cloud of atoms attenuates light passing through it. This attenuation effect can be harnessed by detecting the intensity of light from a laser passing through the atoms, by a CCD camera positioned behind the atom cloud. By analysing the resulting shadow cast by the cloud, valuable insights into the density profile of the atom cloud can be obtained. Especially due to the low mass of lithium atoms, probing them presents challenges, such as detuning due to the Doppler effect or image blurring caused by a random walk process. Such effects highly depend on the imaging laser's intensity, which led to imaging being performed at relatively low intensities compared to the saturation intensity. However, studies have shown that high-intensity absorption imaging offers improved reliability [11]. The central goals of this thesis are therefore understanding and reducing possible noise sources and determining the optimal imaging parameters for our setup.

Firstly, in Chapter 2, I'm going to give a brief overview of the absorption imaging technique as well as the dipole transition within the lithium level structure, that is used for imaging. Following I will introduce a theoretical model for the signal-to-noise ratio (SNR) of our imaging setup in Chapter 3. The aim here is to find the optimal imaging parameters, that maximise the SNR, while also satisfying limitations due to the Doppler effect and a random walk. Chapters 4 and 5 present two approaches to improve our imaging setup. Afterwards chapter 6 deals with experimentally verifying the findings of our noise analysis. Lastly, a conclusion is given in chapter 7.

2. Absorption imaging

To ascertain relevant physical quantities from a cloud of ${}^6\text{Li}$ atoms one typically wants to measure the density distribution. This can be done using the absorption imaging technique. For this approach the atom cloud is placed within a laser beam, appropriately tuned to a designated imaging transition within the lithium level structure. Consequently, the atoms scatter photons and create a shadow behind the cloud, that can be imaged onto a CCD camera. Modelling the atom-light interactions then permits deducing the 2d density integrated along the line of sight.

2.1. Imaging transition

Let us first look at the level structure of ${}^6\text{Li}$. It has a single valence electron giving it a total electronic spin of $s = 1/2$. Employing the central-field approximation to assess all states reveals the two states with the lowest energy, the ground and excited state, denoted as 2S and 2P respectively, which are illustratively depicted in the leftmost column of Figure 2.1. Notably, the transition between these two states manifests as the so-called spectroscopic D-line. This D-line splits into two lines, the D_1 and the D_2 line, when taking coupling between the electronic spin of the valence electron and its orbital angular momentum into account. Then the excited state splits into two fine states ${}^2P_{1/2}$ and ${}^2P_{3/2}$, while the ground state has only one fine state ${}^2S_{1/2}$. This fine structure is schematically indicated in the middle column of Figure 2.1. The figure also shows that the D_1 -line is the spectroscopic feature that results from ${}^2S_{1/2} \leftrightarrow {}^2P_{1/2}$ transitions and the D_2 -line results from ${}^2S_{1/2} \leftrightarrow {}^2P_{3/2}$ transitions. The energy splitting between the two excited states is around 10 GHz [12], which is sufficiently far enough for the two lines to not overlap. This is crucial, because for imaging we only want to drive the D_2 -line transition, exciting the atoms into the ${}^2P_{3/2}$, without exciting them into the ${}^2P_{1/2}$ state. Let us now also consider the hyperfine coupling of the nuclear spin $i = 1$ to the total angular momentum j , which introduces a new quantum number f corresponding to the operator $\hat{\mathbf{F}} = \hat{\mathbf{I}} + \hat{\mathbf{J}}$. Here $\hat{\mathbf{I}}$ is the total nuclear angular momentum operator and $\hat{\mathbf{J}}$ is the total electron angular momentum operator. The quantum number F can therefore take on values in integral steps in the range $|j - i| \leq f \leq (j + i)$.

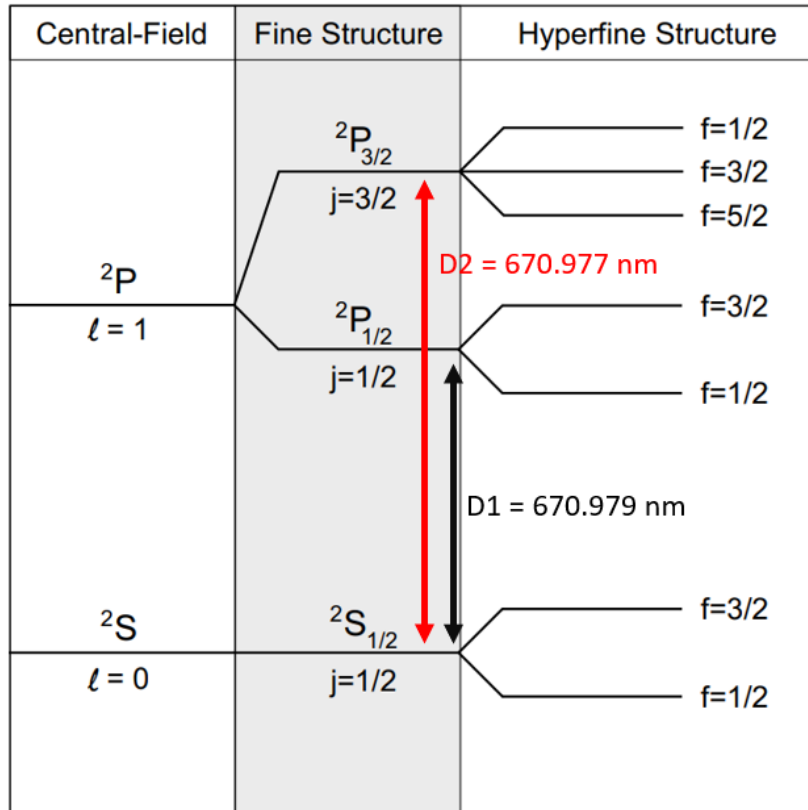


Figure 2.1.: Level structure of ${}^6\text{Li}$ with fine and hyperfine splitting at no magnetic field. Figure taken and adapted from [13]

As shown in the right column of Figure 2.1 the ${}^2S_{1/2}$ state and the ${}^2P_{1/2}$ state therefore split into two hyperfine states with two possible values for the quantum number $f = 1/2, 3/2$. The excited state ${}^2P_{3/2}$ however splits into three states with quantum numbers $f = 1/2, 3/2, 5/2$. Each state comprises $(2f + 1) m_f$ Zeeman sublevels, which are degenerate at zero magnetic field, but split up as we apply an external magnetic field.

Since we are only interested in the D_2 line, let us focus on the ground- and the ${}^2P_{3/2}$ excited state for the following. If a magnetic field is applied and the Zeeman interaction is small compared to the hyperfine splitting, then the Zeeman effect can be treated as a perturbation to the hyperfine states. In this case, the energy splitting goes linear with the B-field.

$$\Delta E_Z = \frac{\mu_B}{\hbar} g_f m_F B \quad (2.1)$$

Here μ_B is the Bohr magneton, B the magnetic field and g_f a Landé g-factor combining

g_i and g_j

$$g_f = g_j \frac{f(f+1) - I(I+1) + J(J+1)}{2f(f+1)} + g_i \frac{f(f+1) + I(I+1) - J(J+1)}{2f(f+1)} \quad (2.2)$$

Since the hyperfine energies for ${}^6\text{Li}$ are small in comparison with other alkalis [13], the linear Zeeman regime only holds for magnetic fields up to a few Gauss. Increasing the magnetic field further leads to the Zeeman interaction getting more and more significant. This causes the energy levels to bend with increasing magnetic field, as can be seen in figure 2.2.

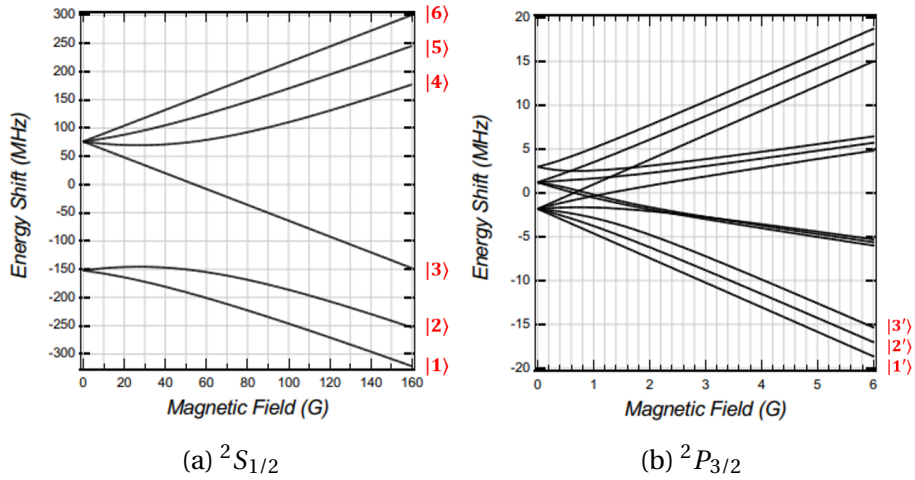


Figure 2.2.: Magnetic-field dependence of the ${}^2S_{1/2}$ ground state (a) and the ${}^2P_{3/2}$ excited state (b) of ${}^6\text{Li}$. Figure taken and adapted from [13].

Eventually, it can no longer be treated as a perturbation and the quantum number f ceases to be a good quantum number. This happens because the nuclear spin and the angular momentum decouple. Finding the eigenstates, in this case, is usually done numerically but can be done analytically for the ground state [14]. One finds the eigenstates in the $|m_j m_i\rangle$ basis

$$\begin{aligned} |1\rangle &= \sin\theta_+ |1/2 0\rangle - \cos\theta_+ |-1/2 1\rangle \\ |2\rangle &= \sin\theta_- |1/2 -1\rangle - \cos\theta_- |-1/2 0\rangle \\ |3\rangle &= |-1/2 -1\rangle \\ |4\rangle &= \cos\theta_- |1/2 -1\rangle + \sin\theta_- |-1/2 0\rangle \\ |5\rangle &= \cos\theta_+ |1/2 0\rangle + \sin\theta_+ |-1/2 1\rangle \\ |6\rangle &= |1/2 1\rangle \end{aligned} \quad (2.3)$$

where $\sin\theta_{\pm}$ and $\cos\theta_{\pm}$ are defined as

$$\begin{aligned}\sin\theta_{\pm} &= \frac{1}{\sqrt{1 + \frac{1}{2}(Z_{\pm} + R_{\pm})^2}} \\ \cos\theta_{\pm} &= \sqrt{1 - \sin^2\theta_{\pm}} \\ Z_{\pm} &= (\mu_n + 2\mu_e) \frac{B}{A_{2S_{1/2}}} \pm \frac{1}{2} \\ R_{\pm} &= \sqrt{Z_{\pm}^2 + 2}\end{aligned}\tag{2.4}$$

with the magnetic dipole constant $A_{2S_{1/2}} = 152.1368407$ MHz [15], the neutron's magnetic moment μ_n and the electron's magnetic moment μ_e . Note that the states are increasingly numbered according to their energy (see figure 2.2). As the magnetic field increases the coefficients $\sin^2\theta_{\pm}$ approach 0, while $\cos^2\theta_{\pm}$ goes to 1, as can be seen in figure 2.3

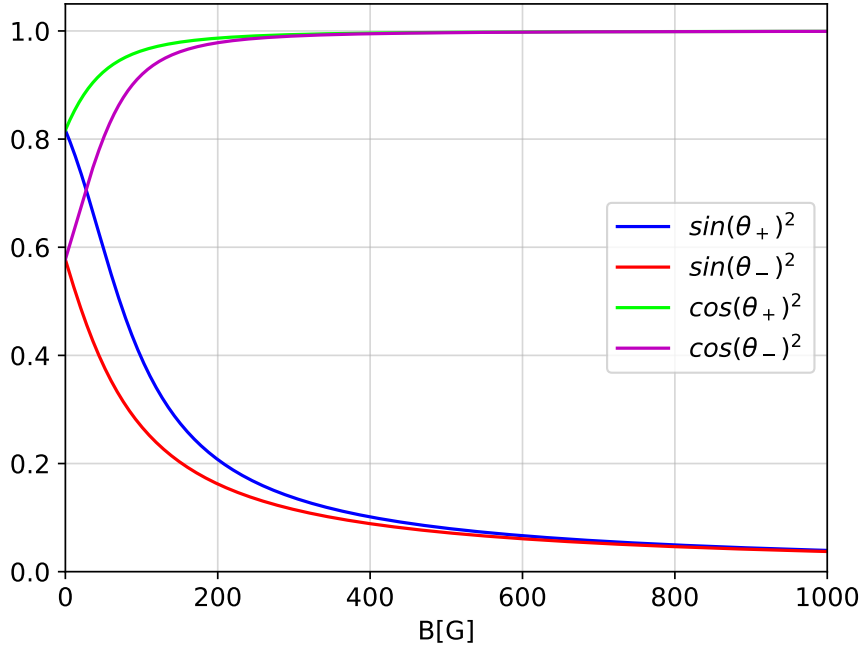


Figure 2.3.: Magnetic-field dependence of the coefficients of states $|1\rangle$ and $|2\rangle$ of the ${}^6\text{Li}$ ground state.

This implies, that for high magnetic fields the ground states can be approximated as

$$\begin{aligned}
 |1\rangle &\rightarrow |{-1/2} \ 1\rangle \\
 |2\rangle &\rightarrow |{-1/2} \ 0\rangle \\
 |3\rangle &= |{-1/2} \ -1\rangle \\
 |4\rangle &\rightarrow |{1/2} \ -1\rangle \\
 |5\rangle &\rightarrow |{1/2} \ 0\rangle \\
 |6\rangle &= |{1/2} \ 1\rangle
 \end{aligned} \tag{2.5}$$

Similarly, we can describe the ${}^2P_{3/2}$ excited state in the $|m_j \ m_i\rangle$ basis. However, this can only be done numerically since there is no analytic form for the different levels. Analogous to the ground state, the nuclear spin and the angular momentum decouple for an increasing magnetic field. But compared to the ground state this decoupling already happens at much lower magnetic field strengths on the order of 1G [16]. Let us now focus only on the three lowest lying excited states, denoted as $|1'\rangle$, $|2'\rangle$ and $|3'\rangle$ (see figure 2.2). For high magnetic fields, they can be expressed in the $|m_j \ m_i\rangle$ basis as found by [16]

$$\begin{aligned}
 |1'\rangle &= |{-3/2} \ -1\rangle \\
 |2'\rangle &\rightarrow |{-3/2} \ 0\rangle \\
 |3'\rangle &\rightarrow |{-3/2} \ 1\rangle
 \end{aligned} \tag{2.6}$$

For now, let us assume an infinitely strong magnetic field, making the approximations in 2.5 and 2.6 exact. The possible dipole transitions are then relatively simple since the selection rules only allow for transitions with $\Delta I = 0$. Consequently, the three lowest lying ground states $|1\rangle$, $|2\rangle$ and $|3\rangle$ get excited by the imaging laser to $|3'\rangle$, $|2'\rangle$ and $|1'\rangle$ respectively, which are the transitions our experiment is conducted with. Figure 2.4 schematically illustrates these relevant transitions.

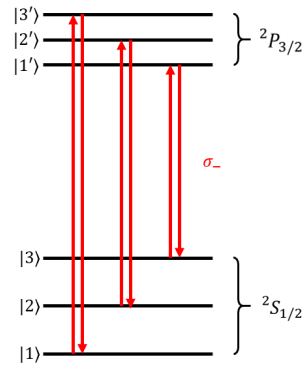


Figure 2.4.: Imaging transition within the D_2 -line for all three ground states.

When introducing a finite magnetic field, the possible transitions become significantly more complicated, because both the ground and excited states have admixtures of other states than the approximation. This causes the risk of the atoms transitioning into states that are off resonant from our imaging laser and therefore don't contribute to the absorption signal anymore. The loss incurred due to these unobservable "dark states" will be explored in detail in the following section.

2.2. Decay into dark states

Every ground and excited state has admixtures of multiple $|m_j m_i\rangle$ states, except the states $|3\rangle$ and $|1'\rangle$. Due to this the dipole transition between $|3\rangle$ and $|1'\rangle$, as can be seen on the right-hand side of figure 2.4, is the only closed transition no matter in which magnetic field. All the other transitions are no closed loops. To account for this we consider the full expressions of the ground states, as described in eq. 2.3. Although also the excited states $|2'\rangle$ and $|3'\rangle$ have admixtures as well, we still use the approximation in eq. 2.6. This is a valid approach, since the excited states already approach their approximation at much lower magnetic field values, such that for a magnetic field of 500G the state $|2'\rangle$ has admixture coefficients on the order of 10^{-6} [16]. Starting from state $|1\rangle$ ($|2\rangle$) an atom gets excited into the state $|3'\rangle$ ($|2'\rangle$). From there the excited state $|3'\rangle = |-3/2 1\rangle$ decays back to the state $|-1/2 1\rangle$, which could either be in state $|1\rangle$ or $|5\rangle$. State $|2'\rangle$ analogously decays to either the state $|2\rangle$ or $|4\rangle$.

$$\begin{aligned} |1\rangle \rightarrow |3'\rangle &= |-3/2 1\rangle \rightarrow |-1/2 1\rangle = \sin\theta_+ |5\rangle - \cos\theta_+ |1\rangle \\ |2\rangle \rightarrow |2'\rangle &= |-3/2 0\rangle \rightarrow |-1/2 0\rangle = \sin\theta_- |4\rangle - \cos\theta_- |2\rangle \end{aligned} \quad (2.7)$$

If the atom decays into the states $|4\rangle$ or $|5\rangle$ depending on the excited state it was in, it no longer contributes to the absorption signal. The probabilities of this happening in each cycle are

$$\begin{aligned} p_{loss}^{1)} &= |\sin\theta_+|^2 \\ p_{loss}^{2)} &= |\sin\theta_-|^2 \end{aligned} \quad (2.8)$$

Since $\sin\theta_{\pm}$ depends on the magnetic field according to eq. 2.4, the loss probabilities decrease with increasing magnetic field, as can be seen in figure 2.5. This implies, that the imaging loops for states $|1\rangle$ and $|2\rangle$ can be closed by increasing the magnetic field.

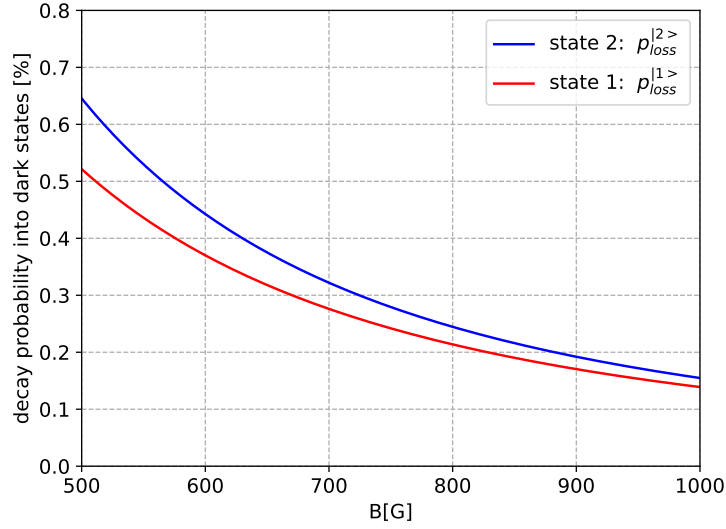


Figure 2.5.: Probability of decay into dark states. Given that the imaging transitions for both states $|1\rangle$ and $|2\rangle$ are not closed, the excited states $|3'\rangle$ and $|2'\rangle$ may decay into states $|5\rangle$ and $|4\rangle$, respectively. These states no longer scatter photons and thus do not contribute to the imaging signal.

Our experiment is conducted at magnetic fields around 890G, at which the loss probabilities become

$$\begin{aligned} p_{loss}^{1\rangle} &= 0.17\% \\ p_{loss}^{2\rangle} &= 0.20\% \end{aligned} \quad (2.9)$$

Since these probabilities are per cycle, the probability of the atom decaying into a dark state during the whole exposure time depends on the number of scattered photons during that time. Depending on the imaging intensity and the exposure time, the number of scattered photons are on the order of 20 (see Chapter 3.1 for details). Therefore the probabilities of losing an atom to a dark state at some point during the exposure time are

$$\begin{aligned} p_{total\ loss}^{1\rangle} &= 3.4\% \\ p_{total\ loss}^{2\rangle} &= 3.9\% \end{aligned} \quad (2.10)$$

Considering that an atom will contribute to the absorption signal up until it decays into a dark state means that the loss in the absorption signal is even lower than the total loss probabilities. Therefore the effect of signal reduction due to a loss to dark states will be neglected in this work. But it needs to be kept in mind especially when working with a weak magnetic field. Before turning to the noise analysis, I want to introduce the Beer-Lambert law and its high-intensity correction.

2.3. Beer-Lambert law

The light from a laser, with the intensity I , propagating along the z direction through a cloud of atoms is attenuated due to photon scattering. This attenuation is described by the Beer-Lambert law:

$$\frac{dI(x, y, z)}{dz} = -n_{3D}(x, y, z)\sigma_{abs}I(x, y, z) \quad (2.11)$$

where n_{3D} is the cloud's density distribution and σ_{abs} the absorption cross-section. Employing this attenuation by imaging the intensity profile behind the cloud onto a CCD camera is called absorption imaging. If the laser intensity approaches the atoms' saturation intensity, eq. 2.11 is modified to

$$\frac{dI(x, y, z)}{dz} = -n_{3D}(x, y, z)\frac{\sigma_{abs}}{1 + s + \delta^2}I(x, y, z) \quad (2.12)$$

with the saturation parameter $s = \frac{I}{I_{sat}}$, where I_{sat} ($25.4 \frac{W}{m^2}$ in the case of ${}^6\text{Li}$) is the saturation intensity. Additionally eq. 2.12 accounts for a possible detuning of the probe laser $\delta = \frac{\omega_L - \omega_0}{\Gamma/2}$, where ω_L , ω_0 and Γ are the laser's angular frequency, the resonant frequency and the natural linewidth. Let us now define the probe's intensity before the cloud $I_{in}(x, y) = I(x, y, z = -\infty)$, after the cloud $I_{out}(x, y) = I(x, y, z = \infty)$, the column density $n_{2D}(x, y) = \int_{-\infty}^{\infty} n_{3D}(x, y, z)dz$, the transmittance $T_{abs}(x, y) = \frac{I_{out}(x, y)}{I_{in}(x, y)}$ and the optical density $OD(x, y) = \sigma_{abs}n_{2D}$. From eq. 2.12 we then find the optical density to be

$$OD(x, y) = -(1 + \delta^2)\log(T_{abs}(x, y)) + s(1 - T_{abs}(x, y)) \quad (2.13)$$

The second term can be neglected in the case of a relatively low probe intensity in comparison with I_{sat} , but for intensities on the order of I_{sat} or higher this correction term becomes relevant.

For absorption imaging one typically acquires three images, measuring the CCD counts $C(x, y)$. One absorption image $C_{abs}(x, y)$ with the atoms and the probe laser on. One division image $C_{div}(x, y)$ without the atoms and the probe beam on and a background image $C_{bac}(x, y)$ without atoms and probe off. The absorption and division images are then corrected by means of subtracting the background counts. In this way, any background stray light is removed.

$$\begin{aligned} C_{out}(x, y) &= C_{abs}(x, y) - C_{bac}(x, y) \\ C_{in}(x, y) &= C_{div}(x, y) - C_{bac}(x, y) \end{aligned} \quad (2.14)$$

Given that $C \propto I$, eq. 2.13 can then be written in terms of CCD counts as

$$OD(x, y) = -(1 + \delta^2) \log \left(\frac{C_{out}(x, y)}{C_{in}(x, y)} \right) + \frac{C_{in}(x, y) - C_{out}(x, y)}{\chi_{sat} \tau} \quad (2.15)$$

Note that here we assumed $C_{sat} = \chi_{sat} \cdot \tau$ to be linear in the exposure time τ , with a time-independent part χ_{sat} . This factor needs to be experimentally calibrated, which will be done in Chapter 6.

3. Noise analysis

Employing a CCD camera for recording absorption imaging signals introduces various noise sources that depend on the imaging parameters such as the relative probe intensity s and the exposure time τ . In order to find the optimal imaging parameters ensuring the highest possible signal-to-noise ratio, this chapter undertakes a theoretical investigation of the influence of these imaging parameters on the signal-to-noise ratio. First, two limitations on the imaging parameters due to photon recoil are introduced in the following sections.

3.1. Doppler shift

During the imaging process, the atoms scatter multiple photons and for each photon they obtain a momentum kick in the propagation direction, gaining a recoil velocity $v_{rec} = \frac{\hbar k}{m}$ per absorbed photon. With the probe laser's wavenumber $k = \frac{2\pi}{\lambda}$, a wavelength of $\lambda = 671\text{nm}$ and a mass of $m = 9.988 \cdot 10^{-27}\text{kg}$ this recoil velocity turns out to be $v_{rec} = 9.89 \frac{\text{cm}}{\text{s}}$ for ${}^6\text{Li}$. Especially due to lithium being extremely light, this recoil velocity is rather high in comparison with other atoms and can therefore not be neglected. Starting with the probe laser on resonance with the imaging transition, each recoil induces a detuning, due to the Doppler effect. So during the entire imaging pulse, the atoms acquire more and more detuning as they scatter multiple photons. The time it takes for the atoms to reach a certain detuning depends on the saturation parameter s , because they scatter more photons for higher probe intensities, leading to a faster accumulation of detuning. Let us define a detuning per photon recoil relative to half the natural linewidth δ_D [17]

$$\delta_D = \frac{v_{rec} k}{\Gamma/2} \quad (3.1)$$

where k is the probe laser's wavenumber and Γ the natural linewidth of the atomic transition. The total detuning δ as a function of time t is then

$$\delta(t) = N_{sc}(t) \delta_D \quad (3.2)$$

with $N_{sc}(t)$, the number of scattered photons after time t . The scattering rate $R_{sc}(t)$ is dependent on the detuning as

$$R_{sc}(t) = \frac{\Gamma}{2} \frac{s}{1 + s + \delta(t)^2} \quad (3.3)$$

which shows that over time as the detuning increases, the atoms will scatter fewer photons. Together with eq. 3.2 one obtains a differential equation for $N_{sc}(t)$, similar to the approach in [18]

$$\frac{d}{dt} N_{sc}(t) = R_{sc}(t) = \frac{\Gamma}{2} \frac{s}{1 + s + N_{sc}(t)^2 \delta_D^2} \quad (3.4)$$

This equation can be solved analytically by separating the variables and assuming that at the initial time $t = 0$ the atoms start with no detuning $\delta(t = 0) = 0$. The full solution can be found in the appendix A.1, while figure 3.1, shows this solution for a range of saturation parameters spanning from 0.1 to 2.

Let us now introduce a limitation to keep the Doppler shift's impact low. We simply force that for the imaging parameters $1 + s > \delta(\tau)^2$ holds, suppressing the influence of δ in eq. 2.12, which gives us a limit for the exposure time, given a saturation parameter. This limit is plotted as a black line in figure 3.3 with the area under this curve satisfying this limit.

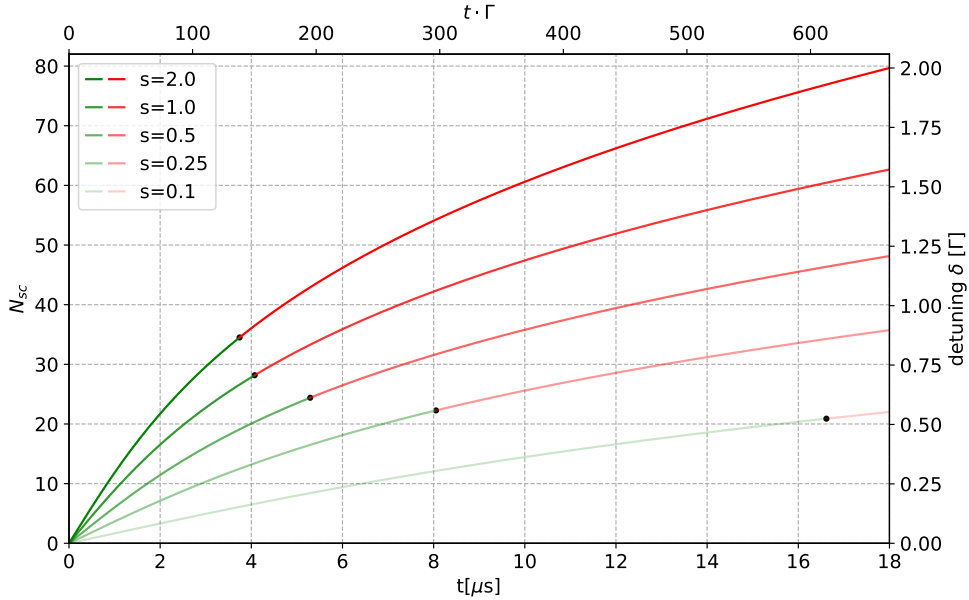


Figure 3.1.: Time dependence of the number of scattered photons per atom for different imaging intensities, calculated analytically from eq. 3.4. The green sections satisfy the Doppler limit, while the red sections do not.

Neglecting the detuning induced by the Doppler effect, we underestimate the number

of atoms from the obtained imaging signal, which could be corrected afterwards. Alternatively one could adjust the probe laser's frequency, such that it is resonant with the atomic transition frequency at all times [19]. Assuming the laser frequency is always resonant with this technique means that the scattering rate as well as the atoms' acceleration is constant. Consequently, the laser frequency needs to be changed linearly with time to compensate for the Doppler detuning.

3.2. Random walk

This chapter addresses the problem of blurring due to the movement of the atoms on the object plane. The excited states of ${}^6\text{Li}$ are not stable, with a lifetime of 27.102 ns [20]. This means around 27.102 ns after absorbing a photon the atoms decay back to the ground state and emit another photon in isotropic directions, giving them a momentum kick. Due to the isotropic property of the spontaneous emission of photons, the atoms undergo a random walk in momentum space, similar to the Brownian motion of microscopic particles. The root mean square velocity v_{rms} resulting from this random walk [21] is

$$v_{rms}(t) = \sqrt{N_{sc}(t)} v_{rec} \quad (3.5)$$

with N_{sc} the number of scattered photons and v_{rec} the recoil velocity as described above. Integrating this velocity over the whole exposure time gives us the root mean square displacement r_{rms} on the object plane.

$$r_{rms} = \int_0^\tau \sqrt{\frac{2}{3}} v_{rms}(t) dt \quad (3.6)$$

Note that this factor of $\sqrt{\frac{2}{3}}$ results from the fact that we are only interested in the displacement on the object plane, which is perpendicular to the direction of the propagating laser. Movement along the direction of the laser doesn't cause the atoms to change pixels and is therefore not relevant in this case. In figure 3.2, this displacement is plotted against the exposure time for different saturation parameters.

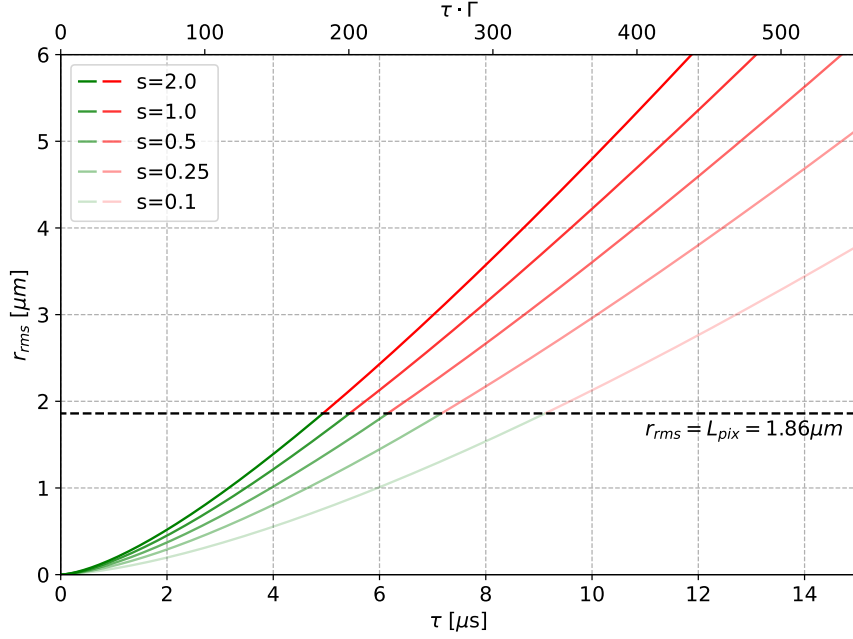


Figure 3.2.: Time dependence of the atoms' displacement after a random walk on the object plane for different imaging intensities, calculated numerically from eq. 3.6. Above the dashed line, the displacement is larger than the pixels, which causes blurring on the image.

To restrain the influence of this random walk, we introduce an upper limit for the displacement r_{rms}

$$r_{rms} < L_{pix} \quad (3.7)$$

where $L_{pix} = 1.86 \mu\text{m}$ is the size of the visual field for one camera pixel at the position of the atoms. From eq. 3.7 we again obtain a limit for the exposure time given a certain saturation parameter, which we compute numerically. In Figure 3.3, this limit is represented by a blue line, with the area beneath the curve satisfying it.

3.3. Optimal imaging parameters

In order to find the optimal imaging parameters, which maximise the OD's signal-to-noise ratio, while also satisfying the limitations described in the two sections above, we introduce a theoretical model for the SNR , following [17]. The SNR is defined as the ratio between the OD and its standard deviation $\overline{\sigma_{OD}}$.

$$SNR = \frac{OD}{\overline{\sigma_{OD}}} \quad (3.8)$$

It's useful to have the transmission T_{abs} as a function of the OD , s and the detuning δ , which we find by inverting eq. 2.15 to be

$$T_{abs} = \frac{(1 + \delta^2)}{s} W\left(\frac{s}{1 + \delta^2} {}^{1+\delta^2}\sqrt{e^{s-OD}}\right) \quad (3.9)$$

with $W()$ denoting the Lambert function. Note that the δ is time-dependent as it is proportional to N_{sc} shown in figure 3.1. Following from eq. 2.15 and using standard error propagation we find the OD's variance to be

$$\sigma_{OD}^2 = (1 + s + \delta^2)^2 \left(\frac{\sigma_{C_{in}}}{\langle C_{in} \rangle}\right)^2 + (1 + sT_{abs} + \delta^2)^2 \left(\frac{\sigma_{C_{out}}}{\langle C_{out} \rangle}\right)^2 \quad (3.10)$$

with $\langle C_{in} \rangle$ and $\langle C_{out} \rangle$ being the mean pixel-wise counts on the division image and the absorption image, respectively. Assuming Poissonian noise, we find

$$\begin{aligned} \langle C_{in} \rangle &= sN_{sat}G_{CCD} \\ \langle C_{out} \rangle &= sN_{sat}T_{abs}G_{CCD} \end{aligned} \quad (3.11)$$

The parameter G_{CCD} characterises the CCD camera's gain, which converts the number of photo electrons (PEs) to counts. However, as this factor ultimately cancels out, its exact value becomes less relevant. Furthermore, we introduced the number of PEs N_{sat} accumulated in the exposure time for $I = I_{sat}$.

For our theoretical model, we consider only the two most dominant noise sources in our system, which are photon shot noise and read out noise [22]. By photon shot noise we mean statistical fluctuations in the number of photons striking the CCD pixels [23], which is a property of the light field itself, rather than an issue of photodetection. To this end, we assume photon shot noise to be Poisson distributed [23], which leads to the variance of impinging photons to be equal to the mean value. The second noise component of importance, read out noise, is a combination of various noise sources that arise from reading out the collected photons [24]. Typically the major contribution to read out noise stems from an on-chip preamplifier and this noise is added uniformly to every pixel. Since the read out procedure is the same for every image, we assume this noise to be independent of the imaging parameters. In the case of our Andor camera it is $\sigma_{RON}^2 = 19.3 e^-/px$ (see appendix A.2), which we add to the photon shot noise according to Gaussian error propagation. We therefore find the variance of the measured counts to be

$$\begin{aligned} \sigma_{C_{in}}^2 &= (sN_{sat} + 2N_{back})G_{CCD}^2 + 2\sigma_{RON}^2G_{CCD}^2 \\ \sigma_{C_{out}}^2 &= (sN_{sat}T_{abs} + 2N_{back})G_{CCD}^2 + 2\sigma_{RON}^2G_{CCD}^2 \end{aligned} \quad (3.12)$$

where N_{back} are the mean background PEs. Note that the factors of 2 emerge from the fact, that C_{in} and C_{out} are composed of two images as described in eq. 2.14. Inserting this into eq. 3.10 we find an expression for the OD's standard deviation as a function of the OD itself, s and time t , which we average over the exposure time τ to find the mean noise to be

$$\overline{\sigma_{OD}} = \frac{1}{\tau} \int_0^\tau \sqrt{\sigma_{OD}^2} dt \quad (3.13)$$

Together with eq. 3.8 we can now numerically compute the signal-to-noise ratio for various imaging parameters. In figure 3.3 I show the signal-to-noise ratio in a relevant parameter space for an OD of 1. It additionally displays the limits discussed in the previous two chapters. The Doppler limit in black and the random walk limit in blue.

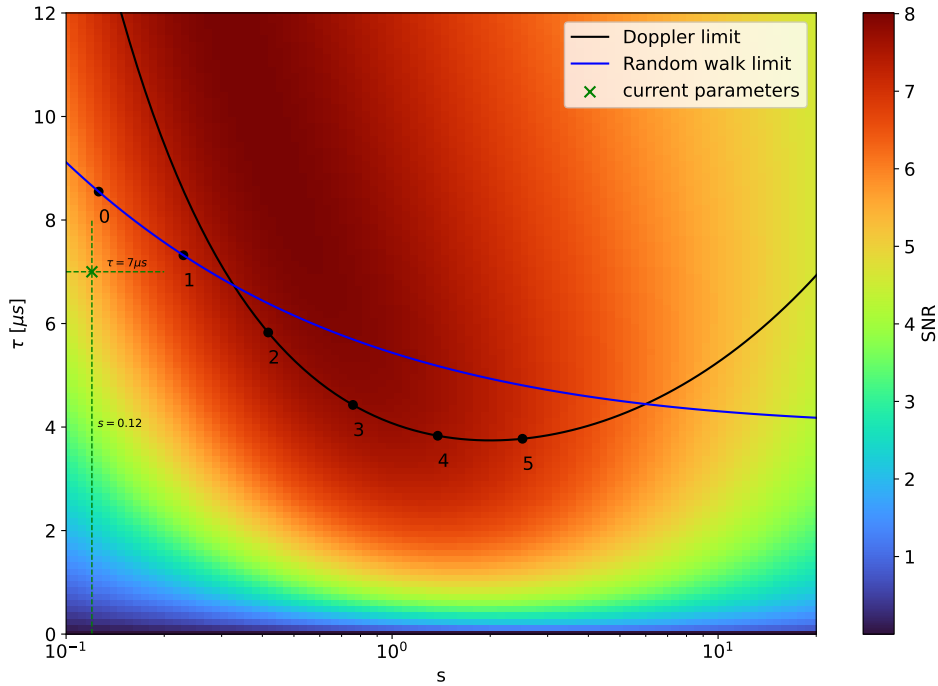


Figure 3.3.: Signal-to-noise ratio for an $OD = 1$ as a function of the imaging parameters saturation s and exposure time τ . The imaging parameters are limited due to a random walk from spontaneous emissions of photons and the Doppler detuning. All parameter configurations below both curves (blue and black) are within those limits. The current setting is marked by the green dashed lines and the 6 dots along the boundary of the two limits numbered 0 to 5 correspond to the curves in figure 3.4

As intuitively anticipated, parameter configurations closest to the limits exhibit the highest signal-to-noise ratio. Now arises the question of whether it is worthwhile to

employ higher imaging intensities compared to the previously used setting (highlighted in green in Figure 3.3). To address this query, we compare the theoretical SNR for our previously employed parameters with a series of six parameter configurations positioned along the boundary of the two limits. These configurations, numbered from 0 to 5 in ascending order of saturation s , are depicted as dots in Figure 3.3. For each configuration, we illustrate the SNR as a function of the OD , as depicted in Figure 3.4.

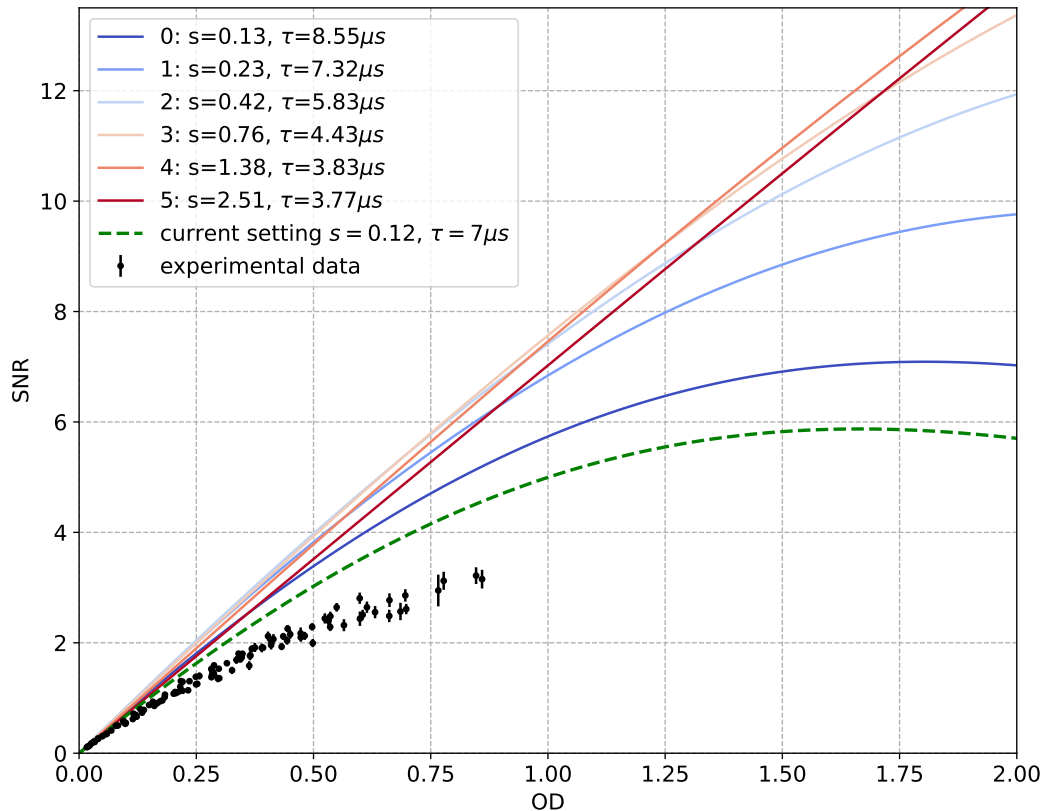


Figure 3.4.: Signal-to-noise ratio as a function of the OD for a set of imaging parameter configurations. The dashed green line is the result of numerically computing the SNR with the currently used imaging parameters. Shown as black dots is experimental data. The most dominant error here is the error from computing the OD s standard deviation from small sets of datapoints (down to 400 points). Especially for higher optical densities, this can lead to a relative error of up to 10%. The curves numbered from 0 to 5 correspond to the points in figure 3.3

Furthermore, Figure 3.4 presents the outcomes derived from experimental data. To obtain these results, we captured multiple images utilising parameters $s = 0.12$ and

$\tau = 7\mu\text{s}$ across diverse dense clouds. Subsequently, we computed the OD using the Beer-Lambert law and fitted each image using a two-dimensional Fermi density distribution function. The fitting process was conducted employing the fitting routine implemented by [22]. Following the fitting procedure, we calculated pixel-wise differences between the fit and the raw data, segmenting them into 12 bins based on the fitted OD value. For each bin, we obtained the standard deviation and its error by means of bootstrapping. For that, we create 1000 boot samples for every bin by randomly selecting pixels within that bin. We then compute the mean of the standard deviation of every boot sample and the standard error. The error of the signal-to-noise ratio can then be determined using Gaussian error propagation. Since the images contain fewer pixels the higher the OD value, the SNR's standard error tends to increase for higher OD values.

Looking at figure 3.4 and comparing the theoretically expected curve (dashed green) with the experimental data points it appears that our theoretical model overestimates the SNR by a factor of approximately 1.2. This has at least two reasons. Firstly, our model only considers photon shot noise and readout noise, which are indeed the most significant noise sources in our system. However, there are additional noise sources that we have not taken into account. For example, dark current noise, which stems from the creation of electron-hole pairs in a pixel due to thermal excitations also contributes to the total noise. Secondly, the saturation parameter $s = 0.12$ could be inaccurately calibrated and overestimated, which would lead to exactly the systematic shift we see.

Finally, we want to identify the optimal imaging parameters for our setup, which maximise the SNR. Based on figure 3.4 we conclude that for our setup saturation values ranging between $s = 0.42$ and $s = 0.76$ coupled with exposure times spanning from $\tau = 5.8\mu\text{s}$ to $\tau = 4.4\mu\text{s}$, corresponding to the curves denoted as 2 and 3 respectively, exhibit the highest SNR within the relevant OD range up to an OD of 1. Given that our experiment isn't expected to extend beyond an optical density of 1, increasing the imaging intensity above $s = 0.76$ would not only yield no additional benefits but might even be counterproductive.

Before we are going to test if these findings can be experimentally verified in chapter 6, we put some effort in enhancing the repeatability of the experimental setup. We start by presenting a implemented power monitoring system, designed to track the imaging pulses, in the following chapter.

4. Fibre monitoring

This chapter gives a summary of a power monitoring setup we implemented. It aims to track the imaging pulses' optical power, which is crucial especially when imaging with high intensities and can be helpful for example to explain possible drifts over time. Furthermore, it can be used to actively stabilise the optical power and to rule out sources of errors that might occur in the experiment. Instead of setting up a free-space photodiode, we implemented a fibre with an already built-in photodiode [25]. This fibre has an optical tap built into the fibre core, which directs 1% of the light passing through the fibre from the core to the cladding surface where it can be directly monitored with a silicon photodiode. This makes setting up very easy since no additional optical components are required, except the fibre.

Reading out the photodiode's signal is relatively simple. The photodiode generates a current proportional to the laser power, which needs to be transformed into a voltage to be measured. Hence we use a combination of a transimpedance amplifier, that performs exactly this conversion and a buffer amplifier, which amplifies the voltage signal further to a reasonable range. Moreover, the buffer amplifier consist of two stages, from which the second stage is optional, which means depending on the strength of the signal one can choose between a channel with a gain of 1 or one with a gain of 50.

Before the fibre was installed into the experimental setup, we performed various test measurements, most importantly one regarding the photodiode's frequency behaviour, in which we modulated the laser power that was coupled into the fibre, using an AOM, with frequencies ranging from 1kHz up to 10MHz. We observed a decrease in the amplitude of the modulated signal for increasing frequencies, as can be seen in figure 4.1. Note that the y-axis is the relative amplitude in dB with the amplitude V_0 at 1kHz as a reference. It is unclear what exactly causes the slight dip at around 20kHz, but it is probably some measurement error unrelated to the actual frequency behaviour of the photodiode. For frequencies higher than 1MHz the signal drops significantly and reaches a -3dB decrease at around 8MHz. This indicates that either the photodiode or the amplifiers are not fast enough for such high frequencies. However since we do not intend to use pulses shorter than $1\mu\text{s}$, corresponding to a frequency of 1MHz this does not affect the pulse monitoring.

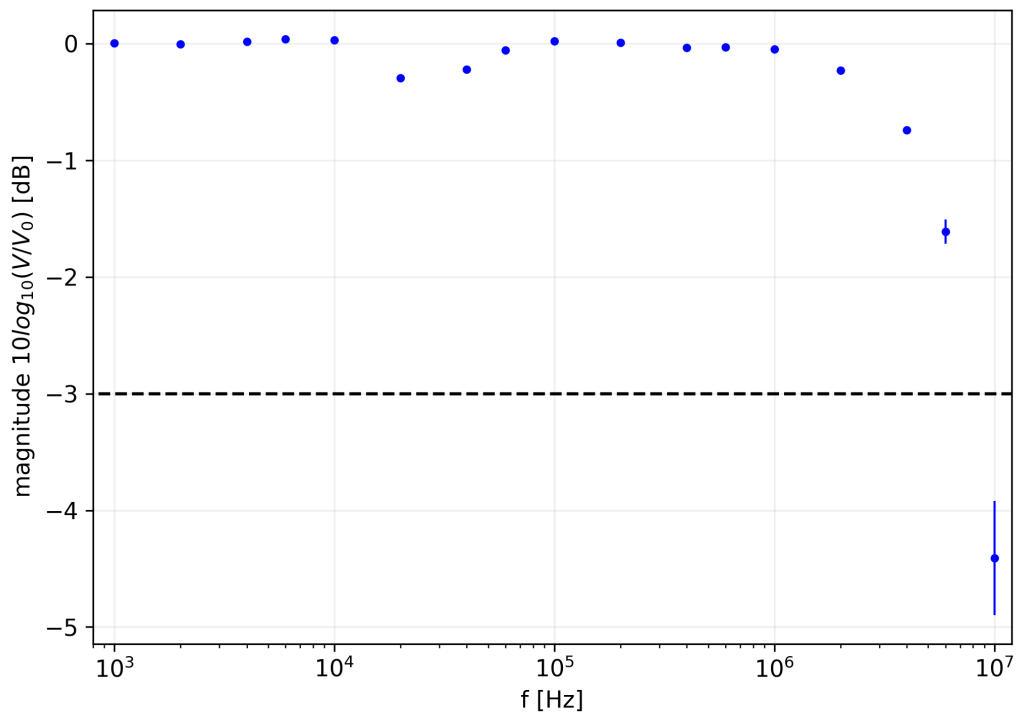


Figure 4.1.: Bode magnitude plot for the inline photodiode and amplifier. A -3dB drop (dashed line) is reached at around 8MHz.

5. Dual Tone AOM

In our imaging setup, the imaging laser pulses are generated by an acousto-optic modulator (AOM). This is done by only using the first order diffracted beam. Pulses can then be generated by switching the radio-frequency (RF) power, driving the AOM, on and off. Figure 5.1 illustrates the integration of the AOM into the optical setup.

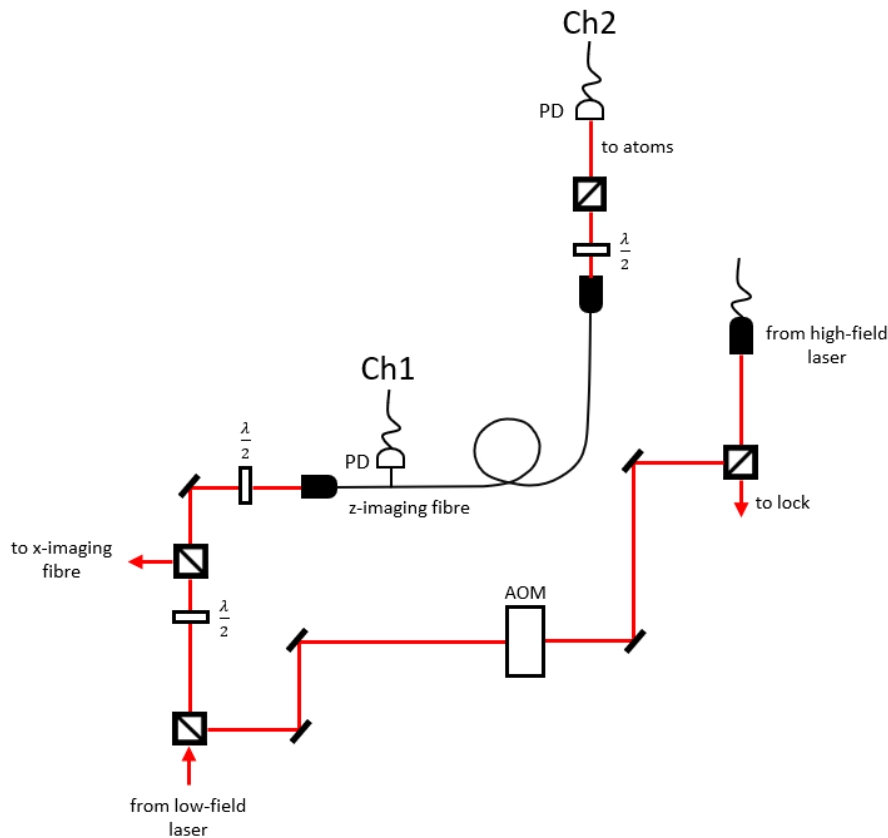


Figure 5.1.: Optical setup of the AOM within the experiment. For the z-imaging fibre, a fibre with an integrated photodiode is employed, enabling tracking of power during the imaging pulses. It's worth noting that the photodiode Ch2 is exclusively utilised for testing purposes and is removed afterwards.

Having constant optical power during imaging pulses and also over longer time scales is crucial to take reliable absorption images but thermal effects inside the AOM's crystal, due to changing the power in the crystal, lead to beam pointing instability up to

1mrad [26]. Because the beam after the AOM is coupled into a fibre, this pointing instability results in a bad coupling efficiency and fluctuating optical power. This chapter therefore addresses this problem and presents a scheme, which aims to compensate these thermal effects.

5.1. Setup for driving the AOM

The approach described in [26] for an AOM driver aims to mitigate thermal effects within the AOM's crystal by maintaining constant RF power within the AOM. To achieve this, the AOM is driven with two frequencies. The primary frequency f_1 , utilised for generating pulses, directs only the first-order diffracted beam into a fibre. The secondary frequency f_2 is adjusted in tandem with the primary frequency to ensure that the RF power remains constant. This ensures, that the AOM remains thermally stabilised. It's worth noting that beams diffracted by the secondary frequency are blocked since its purpose is solely to maintain constant power, and the resulting beams are not utilised.

When driving the AOM with two frequencies, we expect various differently diffracted beams. In contrast to an AOM driven with a single frequency, where one expects beams of the 0th, first, second, and so forth orders, employing two frequencies introduces additional beams arising from the beating frequencies of the two RF signals. For instance, beams corresponding to frequencies $f_2 - f_1$ or $2f_1 - f_2$ are expected to emerge. Figure 5.2 illustrates a few of these beams around the 0th and first order beams.

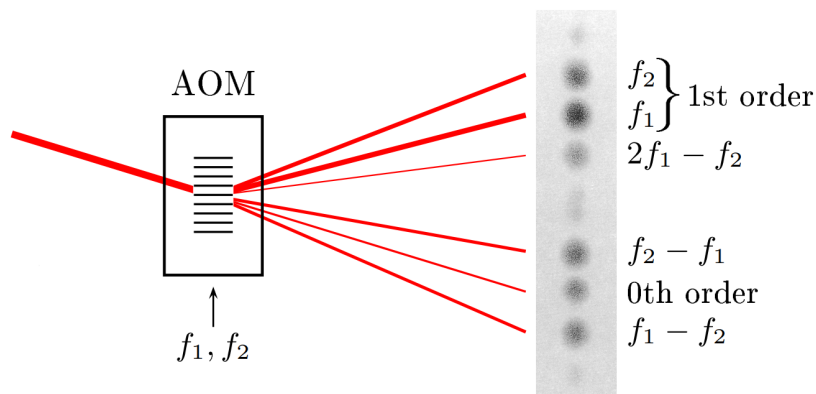


Figure 5.2.: Diffracted beams by an AOM driven by two RF frequencies. This figure is taken and adapted from [26]. The authors used a TeO_2 AOM with approximately the same power for both frequencies to create the image shown on the right-hand side. While multiple beams are generated, all will be dumped except the first order beam of f_1 , which is coupled into a fibre.

In our experiment, only the first order beam of f_1 will be coupled into a fibre and used for the imaging pulses. This means we need to ensure, that this first order beam is spatially separated and does not overlap with any of the other beams, which is done by having enough space, in our case 45cm, between the AOM and the fibre coupler and choosing the RF frequencies far enough from each other. Since the diffracted beams displacement is approximately proportional to the corresponding RF frequency, we aim to separate f_1 and f_2 as far from each other as possible. This ensures maximal separation between the two first-order beams. On the other hand, both frequencies should be well within the AOM's bandwidth, otherwise, most of the RF power would be reflected by the AOM, which could potentially damage the electronic setup of the AOM driver. The AOM's bandwidth was determined by measuring the reflected signal with the help of a R&S ZVL Network Analyser (see appendix A.4 for details). In the end, choosing the two frequencies is always a trade-off between separating the beams far enough and keeping the RF frequencies within the AOM's bandwidth. Additionally we had some trouble with oscillating optical pulse power for some frequencies, which will be discussed in section 5.3. Ultimately we decided the two frequencies to be $f_1 = 110$ MHz and $f_2 = 77.7$ MHz.

Let us now discuss the AOM driver's setup, schematically illustrated in figure 5.3. The optical pulse's power is regulated through an external voltage ranging from 0V to 5V applied to an Arduino. The Arduino then uses a lookup table for the output power and a function approximating the AOM's resonance curve to calculate the power ratio of the two frequencies and outputs 3 voltages controlling the RF power. One for the main frequency, corresponding to the desired optical power and two for the second frequency, from which one is used during the pulses, while the other remains active outside the pulses. Since the Arduino lacks a built-in digital-analog converter, it can only output a pulse width modulated signal, which is why a low pass filter for each output is needed. After the low pass filters, the signal passes through a universal driver for each frequency, that adjusts the dynamic range to match the subsequent component, the variable gain amplifiers. Here the output signals of the VCOs are amplified/attenuated before being sent to a combiner, that combines the two signals. Finally the signal is amplified and sent to the AOM. Controlling the pulses is done with an external TTL signal, which switches the main frequency on and off and switches between the two power control voltages of the second frequency. As a result, when switching the TTL signal from low to high, the main frequency is switched on and the power of the second frequency is adjusted to maintain constant power. Most of the components are e-lego components manufactured by the workshop of the institute, but a full list of all parts is given in appendix A.3.

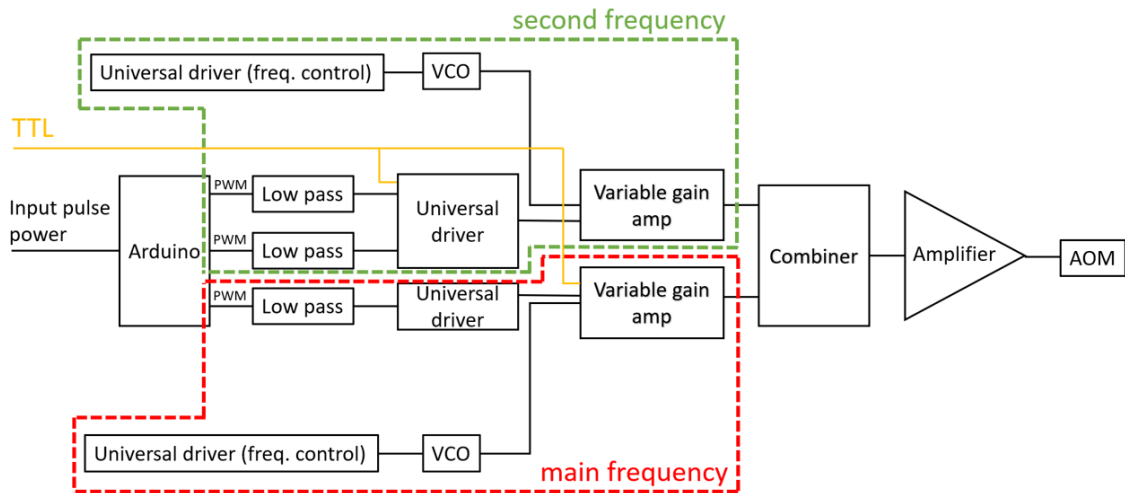


Figure 5.3.: Setup for driving an AOM with two frequencies. To keep the power inside the AOM’s crystal constant, additional to the main RF frequency a second frequency is applied, which compensates for changes in the power of the main frequency. Each RF signal is separately generated by a VCO, on which the frequency is set by a constant control voltage. The power is controlled by an Arduino and set by two variable gain amplifiers. Finally, the two signals are combined, amplified and sent to the AOM.

5.2. Stability of long pulses

As a proof of concept, the first measurements we did were 20s pulses with and without the secondary frequency, to compare the thermalisation process. The results are shown in figure 5.4.

One sees, that without the second frequency (blue) it takes at least 20s until a steady state is reached. In comparison, with the second frequency reaching the steady state is much faster and the pulse’s power starts closer to it. This indicates, that the two-frequency method works as intended and the AOM is constantly thermalised when using the second frequency. However, still with the two frequencies a small thermalisation effect can be seen, which can have multiple reasons. Firstly, the calibration of the RF power could have a systematic error, which would lead to a small change in the power, when switching pulses. Due to this, the AOM’s crystal would have to thermalise to the new power again leading to the slight increase in optical power we observe. Secondly the measurement of the AOM’s bandwidth could have a systematic error leading to the Arduino calculating the RF power wrong. This would have the same effect as an error in the calibration. Lastly, the timing between switching the main RF signal and the second one could be slightly off. Although we use the same TTL signal for both,

there is still a small difference in the time the change reaches the AOM, because the TTL signal is applied at different parts of the circuit, as can be seen in figure 5.3. However, this time difference is estimated to be on the order of 10 ns and can therefore be neglected.

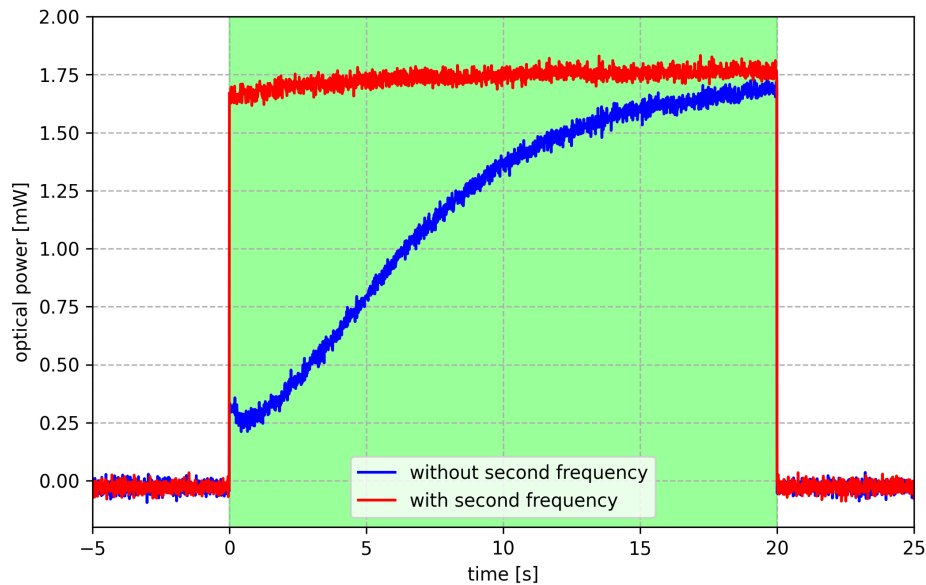


Figure 5.4.: Optical power monitored behind the AOM (Ch1 in Fig. 5.1) during a 20s pulse (green section). The blue curve was measured without the second frequency and it shows an increase of the power by 400% across 20 seconds due to thermal effects. With the second frequency, this increase is reduced to 7%.

An additional improvement to the setup could involve monitoring both the RF power at the amplifier's output as well as the reflected part. This approach would enable the active stabilisation of RF power within the AOM's crystal, further enhancing the pulse's stability.

5.3. Stability of short pulses

In this section, I'm going to present results from measuring the optical power of short pulses at half of the maximum power. This means the RF power inside the AOM's crystal is equally distributed among the two frequencies. Figure 5.5 shows such a pulse for two different second frequencies, where the power was measured behind the imaging fibre (Ch2 in figure 5.1).

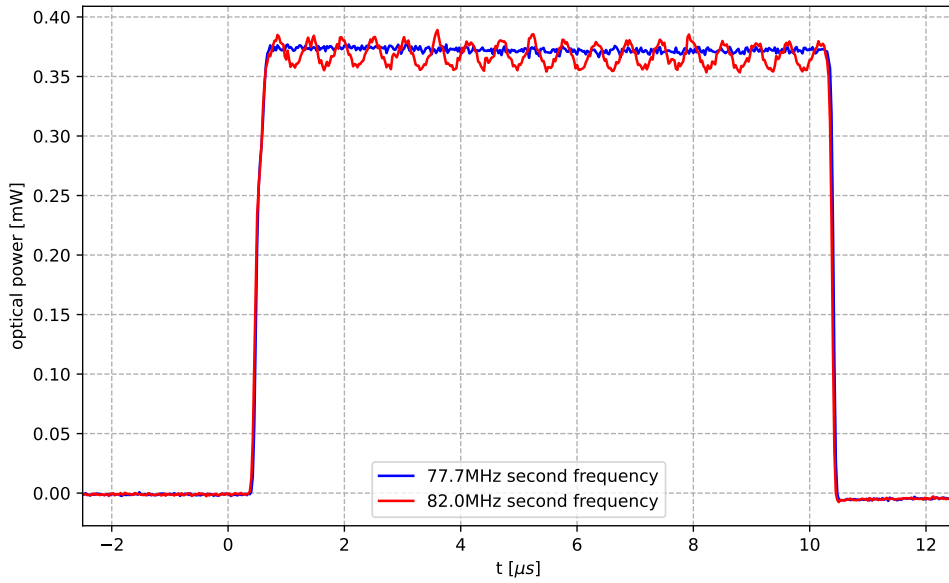


Figure 5.5.: $10\mu\text{s}$ pulses at half the maximum power for different second AOM frequencies recorded behind the z-imaging fibre (Ch2 in figure 5.1). Both pulses were generated with the main AOM frequency at $f_1 = 110\text{MHz}$ but with different second frequencies. The pulse generated with $f_2 = 82.0\text{MHz}$ (red) clearly shows oscillatory behaviour with a frequency of 1.8MHz , while the one with $f_2 = 77.7\text{MHz}$ (blue) does not.

As can be seen the optical power during the pulse oscillates with a frequency of approximately 1.8MHz , when setting the second frequency to $f_2 = 82.0\text{MHz}$. Initially potential overlapping of the two first order beams were suspected to be the source of this oscillation, but this could be ruled out by increasing the distance between the AOM and the fibre coupler to ensure the two first order beams do not overlap. Unfortunately the exact source remains unclear, but we suspect the harmonics of the two RF frequencies to generate this beating phenomenon.

Since maintaining constant optical power throughout the pulse is crucial for reliable imaging signals, a practical workaround solution was implemented by changing the second frequency to $f_2 = 77.7\text{MHz}$. While this does not completely resolve the issue, it shifts the frequency at which the power oscillates to be slow enough for it not to affect pulses on short timescales (on the order of $10\mu\text{s}$), as demonstrated in figure 5.5.

5.4. Long-term drifts

Finally, we sought to observe any potential long-term drifts of the pulse's optical power. To accomplish this, we conducted $10\mu\text{s}$ pulses every 10s over a duration of 16 hours and measured the optical power at various points along the beam path. Therefore a pellicle beamsplitter was introduced into the beam path before the AOM, which reflects about 30% of the beam onto a photodiode, making it possible to observe the optical power before the AOM as a reference. Furthermore, we recorded the power between the AOM and the z-imaging fibre, inside the z-imaging fibre and behind it. Behind the fibre we additionally placed a polarising beam splitter and a photodiode in each of the two resulting beams to also track potential drifts in the polarisation. The results are shown in A.5

Firstly, we observe drifts of the power of approximately 10% regardless of the measurement point along the beam path. Thus these drifts are not an issue of the AOM but rather of the laser and laser locking. Secondly, we noted contrary fluctuations in the two photodiodes behind the fibre, indicating drifts in the polarisation. This stems from misalignment between the polarisation before the fibre and the fibre axis. After a careful alignment, the power fluctuations due to this could be mitigated to a level of about 5%. Lastly we find, that the power measured by the built-in photodiode inside the fibre and the one behind the fibre are very well correlated, as expected. This allows for an active stabilisation of the pulses using the signal of the fibre photodiode. Although the implementation of this stabilisation method falls beyond the scope of this thesis, it represents a crucial step towards improving power stability in future endeavours.

6. Experimental results

From chapter 3 we have gained a theoretical understanding of the signal-to-noise ratio as a function of the imaging parameters, the saturation parameter s and the exposure time τ . We additionally found a range of parameter configurations which optimise the SNR while satisfying certain limits. In this Chapter we aim to experimentally verify these theoretical findings. We therefore vary the imaging parameters, take multiple images of a thermal ${}^6\text{Li}$ cloud for every parameter configuration and calculate the signal-to-noise ratio. The chapter will proceed as follows: Firstly, a description of the measured data will be provided. Secondly, the methodology for calibrating the imaging intensity will be elucidated. Subsequently, I will present a scheme for calculating the signal-to-noise ratio and lastly, the obtained results will be showcased and compared to the theoretical expectation.

Before any images were taken we performed a rough calibration of the saturation parameter. Later this is done much more precisely using the images but as a first estimate, it's enough to measure the total beam power P using a powermeter for various input voltages on the Arduino of the two frequency AOM, which sets the pulse's optical power. The saturation s is then given by [27]

$$s = \frac{2P}{\pi w^2 I_{sat}} \quad (6.1)$$

where I_{sat} is the saturation intensity and w the beam waist, which was approximately determined using a beam profiler to be $w \approx 900\mu\text{m}$. Subsequently, we could start taking images. We scanned through 10 values of the exposure time ranging from $3\mu\text{s}$ to $12\mu\text{s}$ and for every exposure time we scanned through 11 values for the intensity. For each parameter configuration, we took 8 sets of absorption, division and background images.

6.1. Intensity calibration

Because we are reaching saturation values up to $s \approx 2$ during our scan, we need to take the linear correction term in eq. 2.15 into account. This requires to calibrate the counts

per second at the saturation intensity χ_{sat} , which can be done through various methods. For example, one can do this calibration by measuring the momentum transferred to the atoms by the imaging light while varying its intensity [28]. In this work, we instead follow the approach by [17], which will be discussed in this section.

We start by defining $C_1 = -\log\left(\frac{C_{out}}{C_{in}}\right)$ and $C_2 = \frac{C_{in}-C_{out}}{\tau}$. Then solving eq. 2.15 for C_1 , neglecting the detuning δ results in

$$C_1 = OD - \frac{C_2}{\chi_{sat}} \quad (6.2)$$

Since the OD is independent of the imaging parameters, C_1 must be proportional to C_2 with a factor of $-\frac{1}{\chi_{sat}}$. So finding χ_{sat} can be done by measuring C_1 and C_2 , plotting them against each other and fitting a line to the data points. Subsequently, with the fitted χ_{sat} we can calibrate the saturation parameter again

$$s = \frac{C_{in}}{\chi_{sat}\tau} \quad (6.3)$$

The whole calibration is performed only with the images, for which the imaging parameters satisfy both the Doppler limit and the random walk limit, described in Chapter 3. Now with these newly calibrated saturation parameters the images that satisfy these limits might change, which is why we repeat this calibration process until the saturation values don't vary anymore and χ_{sat} reaches a constant value.

In practice, C_1 and C_2 are calculated pixel-wise for every image, that satisfies the two limits. Then a small region of 300 pixels within the cloud's peak is selected, over which we average C_1 and C_2 for each image. Afterwards, we plot the averaged C_1 against C_2 and perform a linear fit. Iterating this process 3 times we obtain the fit displayed in figure 6.1 (red line) and $\chi_{sat} = (215 \pm 23) \mu s^{-1}$, resulting in the saturation parameter ranging from 0.02 to 2 across all images. Finally, we are able to compute the OD according to eq. 2.15 for every image and analyse the signal-to-noise ratio, which will be discussed in the following section.

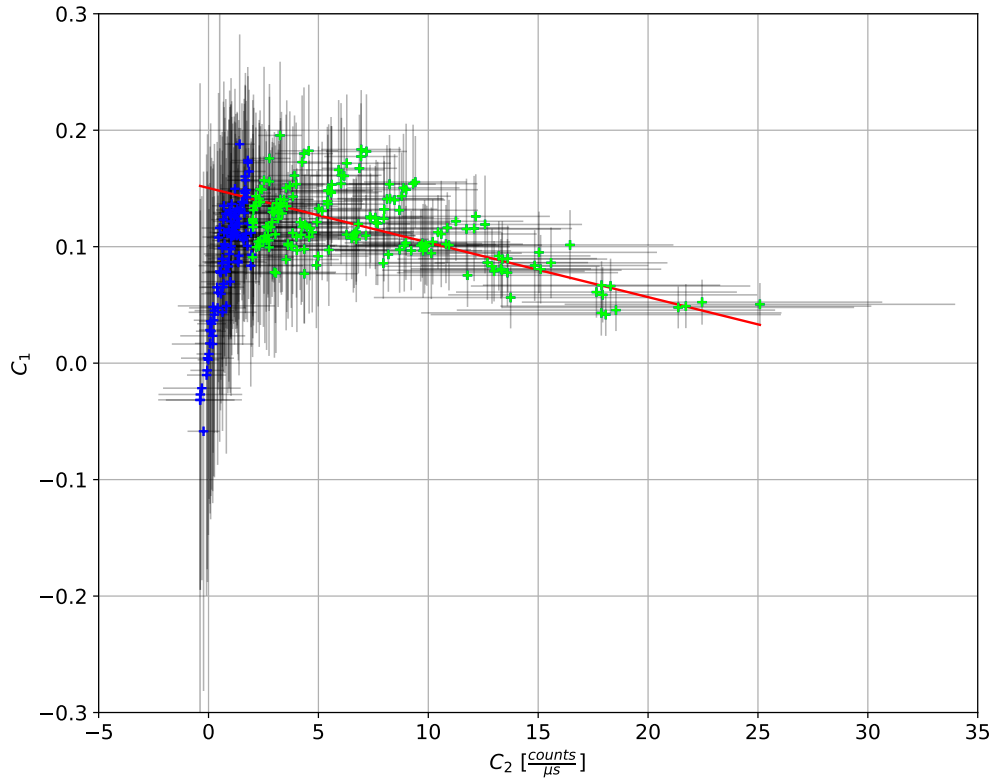


Figure 6.1.: Calibrating χ_{sat} from a linear fit. Each cross corresponds to one image that satisfies the Doppler- and random walk limit with the error bars being the standard deviation of C_1 and C_2 across the 300 pixels they were averaged over. The fit (red line) excludes every image with $C_2 < 2 \frac{\text{counts}}{\mu\text{s}}$ (blue), because this indicates a low and unreliable signal.

6.2. Signal-to-noise ratio and comparison

Now that we have a set of OD images for every parameter configuration we can calculate the signal-to-noise ratio simply by taking the mean and the standard deviation across all images, with the same imaging parameters. Consequently, each pixel is assigned a SNR, as the ratio between the mean OD value and the standard deviation. Afterwards we plot the SNR against the mean OD for every pixel, resulting in a plot, similar to the theory in figure 3.4. For example, figure 6.2 shows the result for the parameters $s = 0.28$ and $\tau = 5\mu\text{s}$. The relatively large spread in the SNR unfortunately stems from the fact, that we calculate the standard deviation with only 8 images.

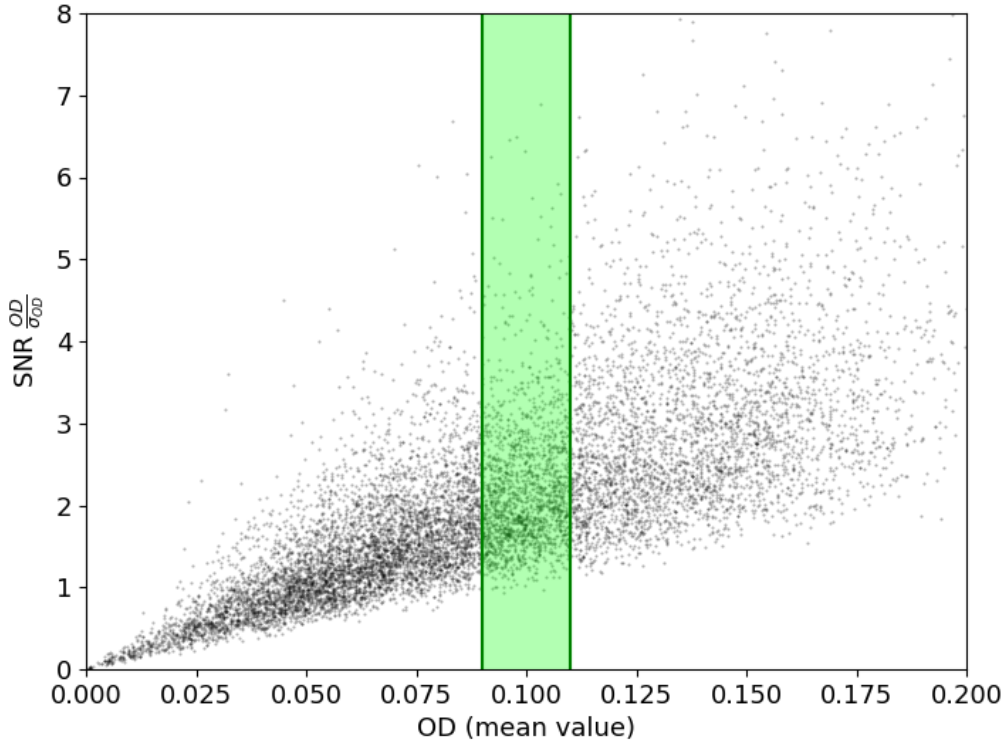


Figure 6.2.: Pixel-wise signal-to-noise ratio as a function of the OD determined experimentally for the parameters $s = 0.28$ and $\tau = 5\mu s$. The pixels within the green area are used to compare different parameter configurations in figure 6.3 by taking the mean SNR in this region.

Nevertheless, to compare different parameter configurations against each other and also against the theoretical results from chapter 3, we focus on a small region between $OD = 0.09$ and $OD = 0.11$ and calculate the mean SNR in that region. The results for all tested parameter configurations are shown in figure 6.3. Note that this comparison includes all imaging parameters, also the ones, that are forbidden according to the two limitations.

Despite the rather large errors, we observe a saturation of the SNR at around $s = 0.75$. This suggests increasing the intensity to $s = 0.75$ would be beneficial in terms of a better SNR, but higher than that would not increase the SNR further. This agrees very well with the predictions from Chapter 3, where we concluded an intensity ranging between $s = 0.42$ and $s = 0.76$ would optimise the SNR. We furthermore observe an increasing SNR for increasing exposure time which also qualitatively agrees with our theoretical model.

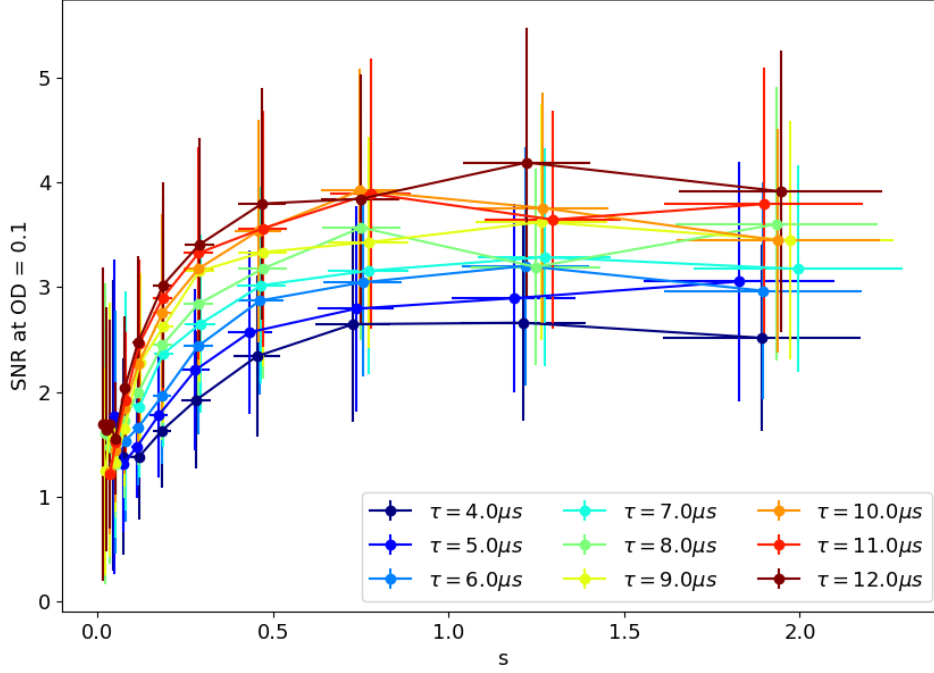


Figure 6.3.: SNR comparison of all parameter configurations. Here the SNR is the mean over all pixels within a small region around a mean OD value of 0.1. As expected the SNR saturates at an intensity of around $s = 0.75$.

Let us now only consider the exposure times $4\mu s$, $5\mu s$ and $6\mu s$ and focus on the saturation parameters, that obey both the Doppler and random walk limit. We again plot the SNR for these exposure times in figure 6.4. For higher exposure times the intensity is limited due to the Doppler- and random walk limit to values below $s = 0.2$ or even lower and since the mean SNR gets increasingly more noisy in this regime, we will only focus on the three exposure times mentioned above. The left-hand side of figure 6.4 shows the experimental results, while the right-hand side displays the theory. Our theory qualitatively aligns with the experimental results, but the measured SNR is unexpectedly larger than predicted by the theory by a factor of 3.3. It's unclear what exactly causes this discrepancy. One possible explanation is the fact, that we are not considering an effective absorption cross-section σ_{abs}^{eff} but rather the theoretical value $\sigma_{abs}^0 = \frac{3\lambda^2}{2\pi}$. Typically, the effective cross-section is smaller than the expected theoretical value, due to factors such as slight deviations in the probe's polarisation. Therefore one usually introduces a correction factor α , which is the ratio between the effective and the theoretical cross-section [17, 11]. It is necessary to calibrate this correction factor, which can be done using the local number density of an ideal non-interacting

Fermi gas as a reference, but is beyond the scope of this thesis. Hence without this calibration our measurement underestimates the OD and given that the SNR is approximately linear for small ODs (see figure 3.4), this would lead to an underestimation of the SNR by our theory.

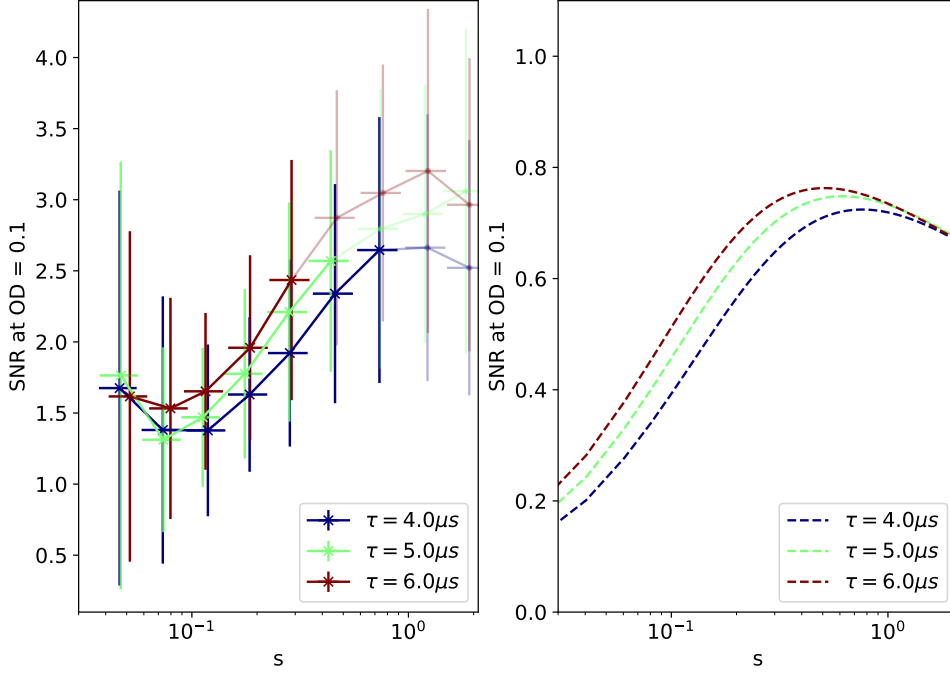


Figure 6.4.: Comparison of the experimentally determined SNR on the left-hand side and the theoretically calculated expectation on the right-hand side. Note that the y-axis scale is different for each diagram. For each exposure time, the saturation parameter is eventually too high for it to fulfil the Doppler and random walk limit. This is indicated by marking the configurations that satisfy both limits with an x and the ones that don't with a dot.

Although we find the experimentally determined SNR to be larger by a factor of ~ 3.3 than the theory, similar to the results from the theory we find the optimal imaging parameters, that maximise the SNR to be the ones closest to the two limits. So in the case of the exposure times $4\mu\text{s}$, $5\mu\text{s}$ and $6\mu\text{s}$ we find the saturation parameters 0.29, 0.44 and 0.73 respectively to maximise the SNR.

This implies using a saturation parameter in the range between 0.29 and 0.73, coupled with an exposure time spanning from $4\mu\text{s}$ to $6\mu\text{s}$, leads to the highest possible SNR. Given the large errors, the measured SNR doesn't differ significantly within these ranges. Hence an exact optimal parameter setting cannot be provided, based only on

the experimental data, but instead I suggest using a configuration within these ranges. Furthermore, several techniques could potentially enhance the SNR further. For example, since the division image is captured without the presence of atoms, there are no constraints on the exposure time. Therefore, it is feasible to increase the exposure time for the division image substantially beyond that used for the absorption image. This adjustment would result in a reduction of noise on the division image. Another approach involves creating bins of pixels either directly using the functionality of the Andor camera or by averaging the measured counts over bins of a certain size. While this approach may lead to a decrease in resolution, it offers a potential gain in the SNR.

7. Conclusion and Outlook

In the first part of this thesis we discussed the method of absorption imaging and looked at the imaging transition for ${}^6\text{Li}$ in detail. We found that for two of the three used ${}^6\text{Li}$ ground states the imaging transition isn't closed and we therefore lose atoms to dark states, that do not contribute to the imaging signal. The loss probability for an atom to decay to such a state highly depends on the magnetic field. For typically used magnetic fields around 890G these probabilities are $p_{loss}^{1\rangle} = 0.17\%$ and $p_{loss}^{2\rangle} = 0.20\%$, depending on the ground state. Based on the number of photons scattered per atom of around 20, we concluded the loss to be negligible.

We then constructed a theoretical model for the SNR of our absorption imaging setup, which takes the two most dominant noise sources into account: photon shot noise and read out noise. Furthermore we considered limitations to the imaging parameters due to the Doppler effect and a random walk. Together with the noise model we found the imaging parameters ranging from $s = 0.42$ to $s = 0.76$ with the exposure time between $\tau = 4.4\mu\text{s}$ and $\tau = 5.8\mu\text{s}$ maximise the SNR, while also satisfying both limits.

Furthermore we implemented two improvements to the setup. A power monitoring system, that uses a fibre with a built-in photodiode to track the imaging laser pulse's power and a two-frequency AOM driver, that reduces thermal effects in the AOM's crystal. With the power monitoring fibre it's possible to explain possible drifts over long time scales, that might occur during measurements. The two-frequency AOM driver stabilises the laser pulse's power by keeping the power inside the AOM constant. We conducted several measurements to characterise the driver. From measuring 20s pulses we showed that the AOM is indeed constantly thermalised. Moreover we unexpectedly observed the pulse's power to be oscillating for a second RF frequency of $f_2 = 82.0\text{MHz}$. This unwanted effect could be reduced by changing to $f_2 = 77.7\text{MHz}$. In addition we examined long-term drifts of the laser power and found them to be approximately 10%. In the future one could implement an active stabilisation of the laser power using the signal of the monitoring fibre, which could eliminate these long-term drifts.

In the last part we performed a scan over the imaging parameters and determined the signal-to-noise ratio for a set of parameter configurations with the aim of comparing it

to the theory constructed previously. At first we calibrated the CCD counts at the saturation intensity to be $\chi_{sat} = 215 \pm 23 \mu s^{-1}$, which is necessary due to the high intensity correction. Afterwards we calculated the SNR for each configuration and compared them against each other and against the theory. As anticipated by the theory we discovered that the SNR saturates for $s > 0.75$, indicating that higher intensities are therefore not worth pursuing. Upon comparing the results to our theory, we observed qualitative agreement, but the exact values differ by a factor of ~ 3.3 . A possible explanation for this discrepancy is the fact, that we aren't accounting for an effective absorption cross-section. Typically one has to independently calibrate a correction factor α , to account for this.

Concluding from both, the theory and the experimental data, we suggest a saturation parameter between $s = 0.29$ and $s = 0.76$, with the appropriate exposure time between $4\mu s$ and $6\mu s$. This ensures the highest possible SNR, while satisfying the Doppler and random walk limit.

A. Appendix

A.1. Number of scattered photons

The time evolution of the number of scattered photons by one atom in a cloud of atoms illuminated by a laser tuned to a specific imaging transition is described by the differential eq. 3.4. Solving this under the assumption of no initial detuning ($\delta(t=0) = 0$) is done by means of separation of the variables. Doing so, one finds the real solution eq. A.1.

$$N_{sc}(t) = \frac{\left(324\delta_D^4\Gamma st + \sqrt{104976\delta_D^8\Gamma^2 s^2 t^2 + 186624\delta_D^6(s+1)^3}\right)^{\frac{1}{3}}}{6 \cdot 2^{\frac{1}{3}}\delta_D^2} - \frac{6 \cdot 2^{\frac{1}{3}}(s+1)}{\left(324\delta_D^4\Gamma st + \sqrt{104976\delta_D^8\Gamma^2 s^2 t^2 + 186624\delta_D^6(s+1)^3}\right)^{\frac{1}{3}}} \quad (\text{A.1})$$

I show this solution for a set of different saturation parameters s in figure 3.1.

A.2. Experimental parameters

The following table summarises relevant experimental parameters for lithium imaging with an Andor iKon camera

property	symbol	value	source
quantum efficiency	Q_E	0.93	[22]
effective pixel size	$L_{pix} [\mu m]$	1.86x1.86	[19]
imaging laser wavelenth	$\lambda [nm]$	671	[19]
saturation intensity of 6Li	$I_{sat} [W m^{-2}]$	25.4	[13]
linewidth of imaging transition	$\Gamma [MHz]$	5.87	[13]
background PE's	N_{back}	30	[29]
read out noise	$\sigma_{ron}^2 [e^- pix^{-1}]$	19.3	Andor camera manual

Table A.1.: Experimental parameters

A.3. AOM driver components

For the dual tone AOM driver the following components were used.

Amount	Description	Model
1	AOM	G&H 3100-125
2	VCO	Mini circuits ZOS-150
1	Arduino	Micro
1	E-lego power supply	DL800
3	Resistor for low pass filter	$R = 33,3k\Omega$
3	Capacitor for low pass filter	$C = 22\mu F$
3	E-lego op amp board	SU805
1	E-lego BNC board	SU802
5	E-lego universal driver	SU804
2	E-lego VGA	SU812
1	Combiner	Mini circuits ZSC-2-1
1	Attenuator	-5dB
1	Amplifier	ZHL-1-2W
1	Power supply for Amplifier	EA-PS-404

Table A.2.: List of AOM driver components

A.4. AOM bandwidth

Every AOM inherently has a bandwidth, which leads to a reflection of the RF signal dependent on its frequency. This effect needs to be taken into account when designing the dual tone AOM driver. More precisely the Arduino controlling the RF powers needs to consider a factor for each frequency when calculating the RF powers. The Arduino controls the power of both RF signals, that reach the AOM. But relevant is only the part that is not reflected by the crystal, which highly depends on the RF frequency, as can be seen in figure A.1. Hence a calibration of the AOM's bandwidth is necessary.

This calibration is simply done by measuring the reflected power using the R&S ZVL Network Analyser. The results are presented in figure A.1. For the two frequencies employed by our dual tone AOM driver, we find the ratios of the power absorbed by the AOM P_{AOM} and the total RF power P_{total} to be

$$\begin{aligned} f_1 = 110\text{MHz} : \frac{P_{AOM}}{P_{total}} &= 96\% \\ f_2 = 77.7\text{MHz} : \frac{P_{AOM}}{P_{total}} &= 80\% \end{aligned} \tag{A.2}$$

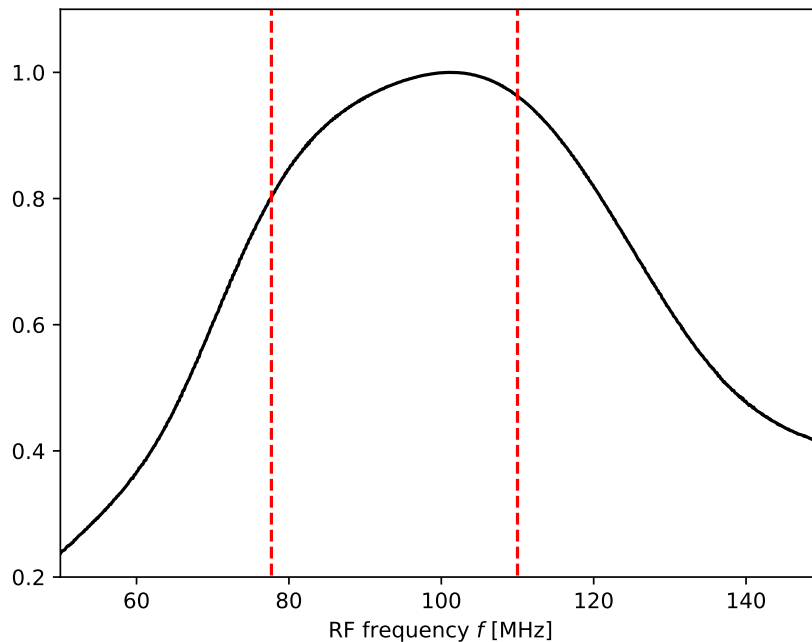


Figure A.1.: Relative power inside the AOM's crystal as a function of the RF frequency. The two red dashed lines mark the two frequencies used by our dual tone AOM driver.

A.5. Long-term drifts

We conducted a measurement concerning long-term drifts as described in section 5.4. The results are presented in figure A.2.

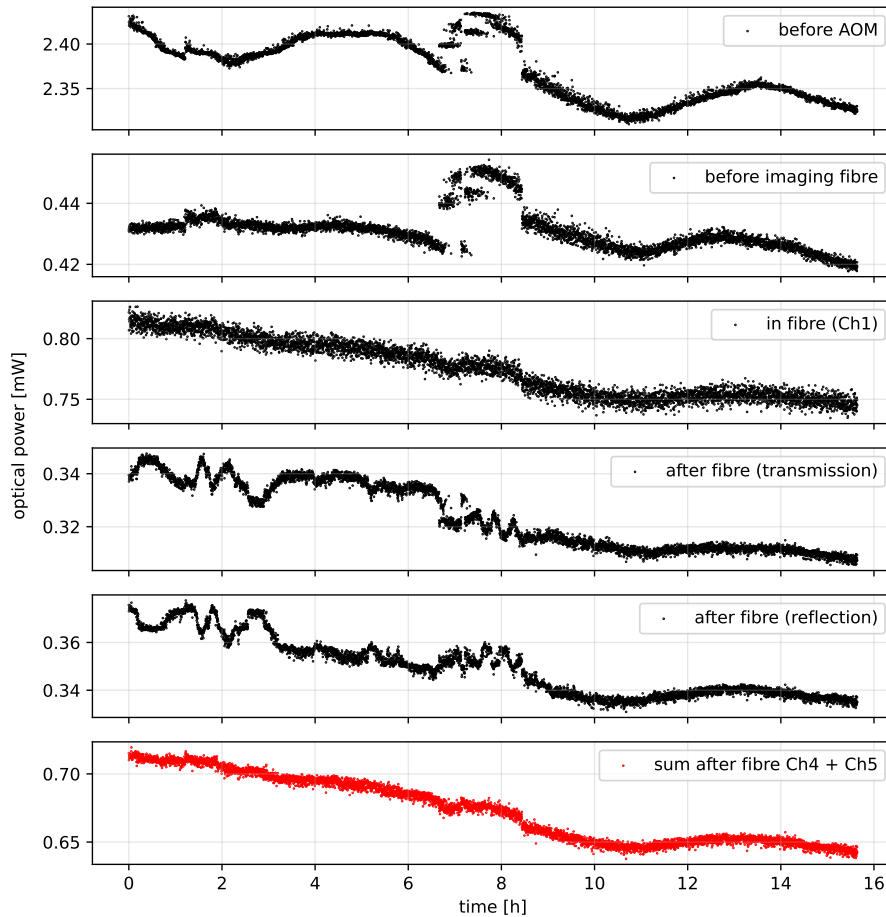


Figure A.2.: Long-term drifts of the pulse's optical power measured at various points along the beam path. From top to bottom, the graphs show the power before the AOM, between the AOM and the fibre, inside the monitoring fibre, transmitted by a polarising beam splitter after the fibre and the reflection of the beam splitter after the fibre. The red dots are the sum of the transmission and reflection after the fibre, combining both polarisations.

Bibliography

- [1] Cheng Chin et al. “Feshbach resonances in ultracold gases”. In: *Reviews of Modern Physics* 82.2 (2010), p. 1225. DOI: 10.1103/RevModPhys.82.1225.
- [2] André Schirotzek et al. “Observation of Fermi polarons in a tunable Fermi liquid of ultracold atoms”. In: *Physical review letters* 102.23 (2009), p. 230402. DOI: 10.1103/PhysRevLett.102.230402.
- [3] Nir Navon et al. “The equation of state of a low-temperature Fermi gas with tunable interactions”. In: *Science* 328.5979 (2010), pp. 729–732. DOI: 10.1126/science.1187582.
- [4] Pietro Massignan, Matteo Zaccanti, and Georg M Bruun. “Polarons, dressed molecules and itinerant ferromagnetism in ultracold Fermi gases”. In: *Reports on Progress in Physics* 77.3 (2014), p. 034401. DOI: 10.1088/0034-4885/77/3/034401.
- [5] Ming-Guang Hu et al. “Bose polarons in the strongly interacting regime”. In: *Physical review letters* 117.5 (2016), p. 055301. DOI: 10.1103/PhysRevLett.117.055301.
- [6] Nils B Jørgensen et al. “Observation of attractive and repulsive polarons in a Bose-Einstein condensate”. In: *Physical review letters* 117.5 (2016), p. 055302. DOI: 10.1103/PhysRevLett.117.055302.
- [7] R Pires et al. “Observation of Efimov resonances in a mixture with extreme mass imbalance”. In: *Physical review letters* 112.25 (2014), p. 250404. DOI: 10.1103/PhysRevLett.112.250404.
- [8] W. Ketterle, D. S. Durfee, and D. M. Stamper-Kurn. *Making, probing and understanding Bose-Einstein condensates*. 1999. DOI: 10.3254/978-1-61499-225-7-67.
- [9] Immanuel Bloch, Jean Dalibard, and Wilhelm Zwerger. “Many-body physics with ultracold gases”. In: *Rev. Mod. Phys.* 80 (3 July 2008), pp. 885–964. DOI: 10.1103/RevModPhys.80.885.
- [10] Erik W Streed et al. “Absorption imaging of a single atom”. In: *Nature communications* 3.1 (2012), p. 933. DOI: 10.1038/ncomms1944.

- [11] G. Reinaudi et al. “Strong saturation absorption imaging of dense clouds of ultracold atoms”. In: *Optics Letters* 32.21 (Oct. 2007), p. 3143. ISSN: 1539-4794. DOI: 10.1364/ol.32.003143.
- [12] J Walls et al. “Measurement of isotope shifts, fine and hyperfine structure splittings of the lithium D lines”. In: *The European Physical Journal D-Atomic, Molecular, Optical and Plasma Physics* 22 (2003), pp. 159–162. DOI: 10.1140/epjd/e2003-00001-5.
- [13] Michael E Gehm. “Properties of ^6Li ”. In: *Jetlab*, (2003).
- [14] M. Houbiers et al. “Elastic and inelastic collisions of ^6Li atoms in magnetic and optical traps”. In: *Physical Review A* 57.3 (1998), R1497–R1500. ISSN: 1094-1622. DOI: 10.1103/physreva.57.r1497.
- [15] E. Arimondo, M. Inguscio, and P. Violino. “Experimental determinations of the hyperfine structure in the alkali atoms”. In: *Rev. Mod. Phys.* 49 (1 1977), pp. 31–75. DOI: 10.1103/RevModPhys.49.31.
- [16] Jan Hendrik Becher. *Towards Spin and Site-Resolved, Single-Atom Imaging of ^6Li Atoms in a Multiwell Potential*. Master’s thesis. 2016.
- [17] Munekazu Horikoshi et al. “Appropriate probe condition for absorption imaging of ultracold ^6Li atoms”. In: *Journal of the Physical Society of Japan* 86.10 (2017), p. 104301. DOI: 10.7566/JPSJ.86.104301.
- [18] Gregory Konstantinidis et al. “Atom number calibration in absorption imaging at very small atom numbers”. In: *Open Physics* 10.5 (2012), pp. 1054–1058. DOI: doi:10.2478/s11534-012-0108-x.
- [19] Melina Filzinger. *Improved manipulation and detection of an ultracold ^6Li - ^{133}Cs mixture towards the investigation of the Bose polaron*. Master’s thesis. 2018.
- [20] WI McAlexander, ERI Abraham, and RG Hulet. “Radiative lifetime of the 2 P state of lithium”. In: *Physical Review A* 54.1 (1996), R5. DOI: 10.1103/PhysRevA.54.R5.
- [21] C.J. Foot. *Atomic Physics*. Oxford Master Series in Physics. OUP Oxford, 2005. ISBN: 9780198506959.
- [22] Felix Clas Borchers. *Modelling of Absorption Imaging of degenerate Fermi Gases in ultracold Atom Experiments*. Bachelor’s thesis. 2023.

- [23] Daniel Durini, ed. *High performance silicon imaging. fundamentals and applications CMOS and CCD sensors*. eng. Woodhead Publishing series in electronic and optical materials ; 60. Cambridge, UK: Woodhead Pub., 2014. ISBN: 978-0-85709-752-1 and 0-85709-752-0.
- [24] Mikhail Konnik and James Welsh. *High-level numerical simulations of noise in CCD and CMOS photosensors: review and tutorial*. 2014.
- [25] OZ Optics. *Directional Fiber oPtic Power Monitors*. Tech. rep.
- [26] B. Fröhlich et al. “Two-frequency acousto-optic modulator driver to improve the beam pointing stability during intensity ramps”. In: *Review of Scientific Instruments* 78.4 (2007). ISSN: 1089-7623. DOI: 10 . 1063/1 . 2720725.
- [27] Bahaa EA Saleh and Malvin Carl Teich. *Fundamentals of photonics*. John Wiley & sons, 2019. ISBN: 9780471839651.
- [28] Klaus Hueck et al. “Calibrating high intensity absorption imaging of ultracold atoms”. In: *Optics express* 25.8 (2017), pp. 8670–8679. DOI: 10 . 1364 / OE . 25 . 008670.
- [29] Michael Rautenberg. *Theoretical considerations concerning the relation of the Efimov scenario to Fermi polarons and upgrade of a polaron experiment*. Master’s thesis. 2021.

Acknowledgments

Many people have helped me in the recent months with all the bigger and smaller problems that I came across. I wholeheartedly want to thank all of you!

First of all, I want to thank Prof. Lauriane Chomaz and Prof. Matthias Weidemüller. I am very grateful to have had the opportunity to work on a very exciting experiment. Throughout the course of this thesis, I was able to learn many interesting things in a very kind and supporting environment.

I would also like to thank Prof. Selim Jochim for kindly agreeing to do the second examination of my thesis.

Besides, I want to thank Michael Rautenberger and Tobias Krom, who never failed to impress me with their profound knowledge as well as their ability and patience to explain anything in ways that were easy to understand. Both of you always made time for me and helped me to make sense of confusing results. I was able to learn a lot from your supervision and in our discussions. Your general tips and opinions on preparing talks and thesis writing were also greatly appreciated.

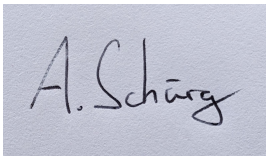
Furthermore I want to thank the whole Mixtures team and former members including Micha, Tobias, Elenora Lippi, Kilian Welz, Finn Mehlhorn and Ron von Oppen. I wish you all the best and eagerly await hearing about exciting developments from the experiment.

Lastly, I am also very thankful to Toni for proof-reading my thesis.

Statement of Authorship

I herewith declare that this thesis was solely composed by myself and that it constitutes my own work unless otherwise acknowledged in the text. I confirm that any quotes, arguments or concepts developed by another author and all sources of information are referenced throughout the thesis. This work has not been accepted in any previous application for a degree.

Heidelberg, 22.04.2024

A rectangular area containing a handwritten signature in black ink on a light blue background. The signature reads "A. Schürg" in a cursive script.

Adrian Schürg